Journal of Power Sources 195 (2010) 6905–6923

Contents lists available at ScienceDirect

Journal of Power Sources

journal homepage: www.elsevier.com/locate/jpowsour

Faradaic impedance of dye-sensitized solar cells

Masayuki Itagaki*, Kazuya Hoshino, Yuya Nakano, Isao Shitanda, Kunihiro Watanabe

Department of Pure and Applied Chemistry, Faculty of Science and Technology, Tokyo University of Science, 2641 Yamazaki, Noda, Chiba 278-8510, Japan

ARTICLE INFO

Article history:
Received 12 March 2010
Accepted 6 April 2010
Available online 10 April 2010

Keywords:
Dye-sensitized solar cell
Faradaic impedance
Electrochemical impedance
Charge transfer resistance
Current–voltage curve

ABSTRACT

Theoretical equations of the Faradaic impedance of the photoelectrode and the counter electrode of dye-sensitized solar cell (DSC) were derived. The Faradaic impedance is the frequency dependent resistance related to the time constants of elementary electrode processes like photoexcitation, electron transfer, charge transfer reaction and diffusion. The typical cell impedance spectrum describes the locus of three semicircles on the Nyquist plane. The locus of three semicircles is generally analyzed by using the equivalent circuit composed of charge transfer resistance ($R_{ct,1}$) and capacitance ($C_{dl,1}$) of counter electrode, charge transfer resistance ($R_{ct,2}$) and capacitance ($C_{dl,2}$) of photoelectrode, the finite diffusion impedance due to the diffusion of I_3^- on the counter electrode (Z_w), and total resistance of the substrate and solution (R_s). The physical meanings of $R_{ct,1}$ and $R_{ct,2}$ can be elucidated by the interpretations of Faradaic impedance derived in the present paper. The $R_{ct,1}$ is represented as the function of the potential-dependent rate constants of I_3^- reduction and I^- oxidation. On the other hand, the $R_{ct,2}$ is the function of the photoelectrode potential, the surface concentration of I_3^- and the potential-independent rate constant of the back electron transfer reaction. The theoretical expressions of the current–voltage (I–V) curve of the DSC can be also derived. In the present paper, the relations between the impedance and I–V curve of the DSC are discussed.

1. Introduction

Dye-sensitized solar cell (DSC) is expected to be energy device in the next generation because of various advantages such as simple manufacturing process, low cost and low environmental loading [1–3]. Recently, it was reported that any compact cells achieved electrical energy conversion efficiencies of more than 10% [4–6]. The modularization technology has been also developed. Toyoda et al. [7] fabricated large scale DSC modules with glass substrate, and indicated that the modules have the long term stability for a half year. Ikegami et al. [8] reported that a plastic DSC module maintained its high conversion efficiency under the accelerated condition of 55 °C and 95% relative humidity.

Typical DSC is composed of three parts shown as follows [9].

(1) Photoelectrode (anode) which consists of a porous TiO_2 film with adsorbed dye and the fluorine-doped SnO_2 (FTO) substrate.
(2) Organic electrolyte solution containing redox couples such as iodide ions (I^-)/triiodide ions (I_3^-).
(3) Pt or carbon counter electrode (cathode).

During the illumination of the cell, electrons are injected from the photoexcited dye into TiO_2 film and diffuse in the TiO_2 conduction band. These electrons pass through FTO substrate and then through the external circuit. At the same time, the oxidized dye, which is generated by the photooxidation reaction, is reduced by charge transfer reaction with I^-. I_3^- is fomed by the charge transfer reaction on the photoelectrode and diffuses to the counter electrode where I_3^- is reduced back to I^-. Since the electrons circulate through the cell, the light energy is converted into the electrical energy.

Charge recombination, which is the major factor that limits the cell performance, is also occurred at the photoelectrode interface. For example, the electron injected in the TiO_2 film may recombine with oxidized dye and react with I_3^- [10].

The analysis of the reaction processes in the DSC is very important for the characteristic improvement of the cell. Therefore, reaction processes of DSC have been investigated by using electrochemical impedance spectroscopy (EIS) as well as intensity modulated photocurrent spectroscopy (IMPS) [11,12] and intensity modulated photovoltage spectroscopy (IMVS) [12,13]. EIS is one of the nondestructive methods measuring the current response to the application of sinusoidal AC voltage at various frequencies. The EIS can discriminate the charge transfer that is fast reaction process and diffusion that is slow process by the discrimination of their time constants. Therefore, EIS is applicable to various fields such as corrosion, electroplating, secondary battery and electrochemical capacitor [14–17].

* Corresponding author. Tel.: +81 4 7122 9492; fax: +81 4 7123 9890.
E-mail address: itagaki@rs.noda.tus.ac.jp (M. Itagaki).

0378-7753/$ – see front matter © 2010 Elsevier B.V. All rights reserved.
doi:10.1016/j.jpowsour.2010.04.014

Nomenclature

b_3 [V^{-1}] Tafel constant of k_3
b_{-3} [V^{-1}] Tafel constant of k_{-3}
$c_{I_3^-,a}$ [mol cm^{-3}] concentration of I_3^- on photoelectrode
$c_{I^-,a}$ [mol cm^{-3}] concentration of I^- on photoelectrode
$c^*_{I_3^-,a}$ [mol cm^{-3}] bulk concentration of I_3^- on photoelectrode
$c^*_{I^-,a}$ [mol cm^{-3}] bulk concentration of I^- on photoelectrode
$\bar{c}_{I_3^-,a}$ [mol cm^{-3}] steady-state value of $c_{I_3^-}$ on photoelectrode
$\bar{c}_{I^-,a}$ [mol cm^{-3}] steady-state value of c_{I^-} on photoelectrode
$c_{I_3^-,c}$ [mol cm^{-3}] concentration of I_3^- on counter electrode
$c_{I^-,c}$ [mol cm^{-3}] concentration of I^- on counter electrode
$c^*_{I_3^-,c}$ [mol cm^{-3}] bulk concentration of I_3^- on counter electrode
$c^*_{I^-,c}$ [mol cm^{-3}] bulk concentration of I^- on counter electrode
$\bar{c}_{I_3^-,c}$ [mol cm^{-3}] steady-state values of $c_{I_3^-}$ on counter electrode
$\bar{c}_{I^-,c}$ [mol cm^{-3}] steady-state values of c_{I^-} on counter electrode
c_0 [cm s^{-1}] light speed
C_1 [F cm^{-2}] capacitance of counter electrode
C_2 [F cm^{-2}] capacitance of photoelectrode
$C_{dl,a}$ [F cm^{-2}] electric double layer capacitance of photoelectrode
$C_{dl,c}$ [F cm^{-2}] electric double layer capacitance of counter electrode
$D_{I_3^-}$ [cm^2 s^{-1}] diffusion coefficient of I_3^-
D_{I^-} [cm^2 s^{-1}] Diffusion coefficient of I^-
E_a [V] conduction band energy level in semiconductor bulk
E_c [V] potential of counter electrode
E_{eq} [V] equilibrium potential of counter electrode
E_{fb} [V] flat band potential of photoelectrode
$E_s(\lambda)$ [J] light intensity at λ under the reference solar spectral irradiance
E_λ [J] energy per one photon at λ
$\vec{E}$ [V cm^{-1}] electric field in space charge layer
F [C mol^{-1}] Faraday constant
G [mol cm^{-2} s^{-1}] electron excitation rate under light illumination of photoelectrode
G_0 [mol cm^{-2} s^{-1}] electron excitation rate under light illumination of photoelectrode without oxidized dye
h [J s] Planck constant
h_1 [cm] reaction layer thickness of electrochemical reactions on photoelectrode
h_2 [cm] thickness of TiO_2 film surface layer
h_3 [cm] reaction layer thickness of electrochemical reactions on counter electrode
I [A cm^{-2}] current density
$I_0(\lambda)$ [mol cm^{-3}] light intensity at single wavelength of photon
$J_{I_3^-,a}$ [mol cm^{-2} s^{-1}] flux of I_3^- on photoelectrode
$J_{I^-,a}$ [mol cm^{-2} s^{-1}] flux of I^- on photoelectrode
$J_{I_3^-,c}$ [mol cm^{-2} s^{-1}] flux of I_3^- on counter electrode
$J_{I^-,c}$ [mol cm^{-2} s^{-1}] flux of I_3^- on counter electrode
k_1 [cm^7 mol^{-2} s^{-1}] rate constant of oxidation of I^- on photoelectrode
k_2 [cm^4 mol^{-1} s^{-1}] rate constant of reduction of I_3^- on photoelectrode
k_3 [cm s^{-1}] potential-dependent rate constant on counter electrode
k_{-3} [cm^7 mol^{-2} s^{-1}] potential-dependent rate constant on counter electrode
k_3' [cm s^{-1}] rate constant ($E_c = 0$)
k_{-3}' [cm^7 mol^{-2} s^{-1}] rate constant ($E_c = 0$)
n_0 [mol cm^{-2}] surface concentration of adsorbed dye
n_s [mol cm^{-3}] electron density in TiO_2 film
$\bar{n}_s$ [mol cm^{-3}] Steady-state values of n_s
N_A [mol^{-1}] Avogadro's number
N_D [cm^{-3}] donor density
N_0 [mol cm^{-3}] electron density in TiO_2 film at $V_{oc} = 0$
q [C] elementary charge
R [J K^{-1} mol^{-1}] gas constant
$R_{ct,1}$ [Ω cm^{-2}] charge transfer resistance of counter electrode
$R_{ct,2}$ [Ω cm^{-2}] charge transfer resistance of photoelectrode
R_p [Ω cm^{-2}] polarization resistance of cell impedance
R_s [Ω cm^{-2}] total resistance of substrate and solution
$R_{h,a}$ [Ω cm^{-2}] high frequency limit of $Z_{F,a}$
$R_{h,c}$ [Ω cm^{-2}] high frequency limit of $Z_{F,c}$
$R_{m,a}$ [Ω cm^{-2}] resistance of the intersection point on the real axis of $Z_{F,a}$ in middle frequency range
$R_{l,a}$ [Ω cm^{-2}] low frequency limit of $Z_{F,a}$
$R_{l,c}$ [Ω cm^{-2}] low frequency limit of $Z_{F,c}$
$R_{diff,a}$ [Ω cm^{-2}] diffusion resistance of photoelectrode
$R_{diff,c}$ [Ω cm^{-2}] diffusion resistance of counter electrode
T [K] absolute temperature
v_1 [mol cm^{-2} s^{-1}] oxidation rate of I^-
v_2 [mol cm^{-2} s^{-1}] reduction rate of I_3^-
V_{oc} [V] open circuit voltage
W [cm] thickness of space charge layer
Z_a [Ω cm^{-2}] impedances of photoelectrode
Z_c [Ω cm^{-2}] impedances of counter electrode
Z_{DSC} [Ω cm^{-2}] cell impedance
$Z_{F,a}$ [Ω cm^{-2}] Faradaic impedance of photoelectrode
$Z_{F,c}$ [Ω cm^{-2}] Faradaic impedance of counter electrode
Z_w [Ω cm^{-2}] finite diffusion impedance
$\alpha_{abs}(\lambda)$ [cm^{-1}] absorption coefficient of the dye at λ
δ_a [cm] diffusion layer thickness on photoelectrode
δ_c [cm] diffusion layer thickness on counter electrode
ϕ effective permeability of light of photoelectrode
η_a [V] overvoltage at I of photoelectrode
η_c [V] overvoltage at I of counter electrode
κ_s [F cm^{-1}] dielectric constant
λ [cm] wavelength of photon
μ [cm^2 V^{-1} s^{-1}] electron mobility in TiO_2 film
θ ratio of the oxidized dye
$\bar{\theta}$ steady-state values of θ
$\tau_{h,a}$ [s] time constant of semicircle of $Z_{F,a}$ in high frequency range
$\tau_{l,a}$ [s] time constant of finite diffusion impedance of $Z_{F,a}$
$\tau_{l,c}$ [s] time constant of finite diffusion impedance of $Z_{F,c}$
$\tau_{semi,a}$ [s] time constant of semicircle of Z_a
$\tau_{semi,c}$ [s] time constant of semicircle of Z_c
ω [s^{-1}] angular frequency

EIS have also been used for analyses on DSC [8,9,12,18–104]. The characteristics of DSC [8,9,18–35], photoelectrode [5,12,36–67], counter electrode [68–79], electrolyte [80–98], substrate [70,99–104] and degradation process [8,9,27,30–32,76] are investigated by EIS. Hoshikawa et al. [19,21] measured three

impedance spectra of photoelectrode, counter electrode and DSC by using a reference electrode inserted directly into the DSC. Typical electrochemical impedance of DSC describes three semicircles on the Nyquist plane [9]. It was reported that the three semicircles were attributed to the redox reaction at the electrolyte/counter electrode interface (high frequency region), the charge transfer reaction at the TiO_2/electrolyte interface (middle frequency region) and electrolyte diffusion (low frequency region) [12].

Fig. 1 shows five equivalent circuits which have been proposed for impedance analyses of DSC. The equivalent circuit in Fig. 1(a) is composed of five parameters as follows: total resistance of the substrate and solution (R_s), charge transfer resistance ($R_{ct,1}$) and capacitance (C_1) of counter electrode, charge transfer resistance ($R_{ct,2}$) and capacitance (C_2) of photoelectrode and the diffusion impedance of I_3^- on the counter electrode (Z_w) [35,53,77,98]. The equivalent circuit in Fig. 1(b) is composed of the contact resistance of FTO/TiO_2 interface (R_{FTO/TiO_2}) and the capacitance of this interface (C_{FTO/TiO_2}) in addition to that in Fig. 1(a) [34]. Grätzel et al. [9,29] suggested the equivalent circuit shown in Fig. 1(c). Z_e is a diffusion element at the TiO_2/electrolyte interface [9]. The equivalent circuits shown in Fig. 1(b) and (c) might be able to explore the characteristics of DSC in detail by comparing with that shown in Fig. 1(a). As above-mentioned, three semicircles are often observed in the Nyquist plots of the typical experimental results of EIS. In this case, all parameters of the equivalent circuits in Fig. 1(b) and (c) could not be decided by curve-fitting. In Fig. 1(d), transmission line model (TLM) is introduced in the equivalent circuit. The lumped constant equivalent circuit cannot be used for the curve-fitting of impedance spectra when the current distribution occurs inside the pore of porous electrode. The TLM is well known to present the electrochemical property of porous electrode. Some researchers investigated the current distribution in the porous TiO_2 electrodes by using the equivalent circuit shown in Fig. 1(d) [80]. Han et al. [18] proposed the equivalent circuit shown in Fig. 1(e) in which a diode element and a shunt resistance are included. They claimed that the resistance element related to charge transport at the TiO_2/dye/electrolyte interface displays behavior like that of a diode, and that the series resistance element corresponds to the sum of the other resistance elements.

The theoretical calculations of impedance for DSC are also reported [12,25,36,37,40,41]. Many of them are derived from the fact that diffusion of the electrons in the conduction band of TiO_2 obeys Fick's second law. Bisquert [37] derived the theoretical impedance formula based on the following three assumptions: (1) electrons diffuse in the TiO_2 film, (2) there is not trap level in TiO_2 and (3) charge recombination reaction is first-order reaction. On the other hand, Kern et al. [12] derived the theoretical impedance formula based on the following three assumptions: (1) light illumination provides the generation of electrons injected into the conduction band of TiO_2 due to the sensitization by the dye, (2) only a single trap level is assumed and the rate constant for the trapping of the conduction band electrons is much faster than the rate constant for the detrapping of the electrons, and (3) the recombination rate of the trapped electrons with I_3 is second order. Adach et al. [25] found that the identical equation was derived from two different impedance models which are proposed by Kern et al. [12] and Bisquert [37] under specific assumptions. In addition, Adach et al. [25] discussed the reason why these two different impedance formula are attributed to the identical equation. However, these theoretical analyses [12,25,36,37,40,41] suffer at least two disadvantages: one is that the redox reaction of the electrolyte such as I^-/I_3^- is not considered on the photoelectrode, and the other is that the effect of light intensity is not reflected on the impedance spectra.

Ferber et al. [105] presented a theoretical model for current–voltage (I–V) curve simulation of DSC. They considered the redox reaction of the electrolyte and electron transfer to the TiO_2 conduction band in the theoretical model. This model can

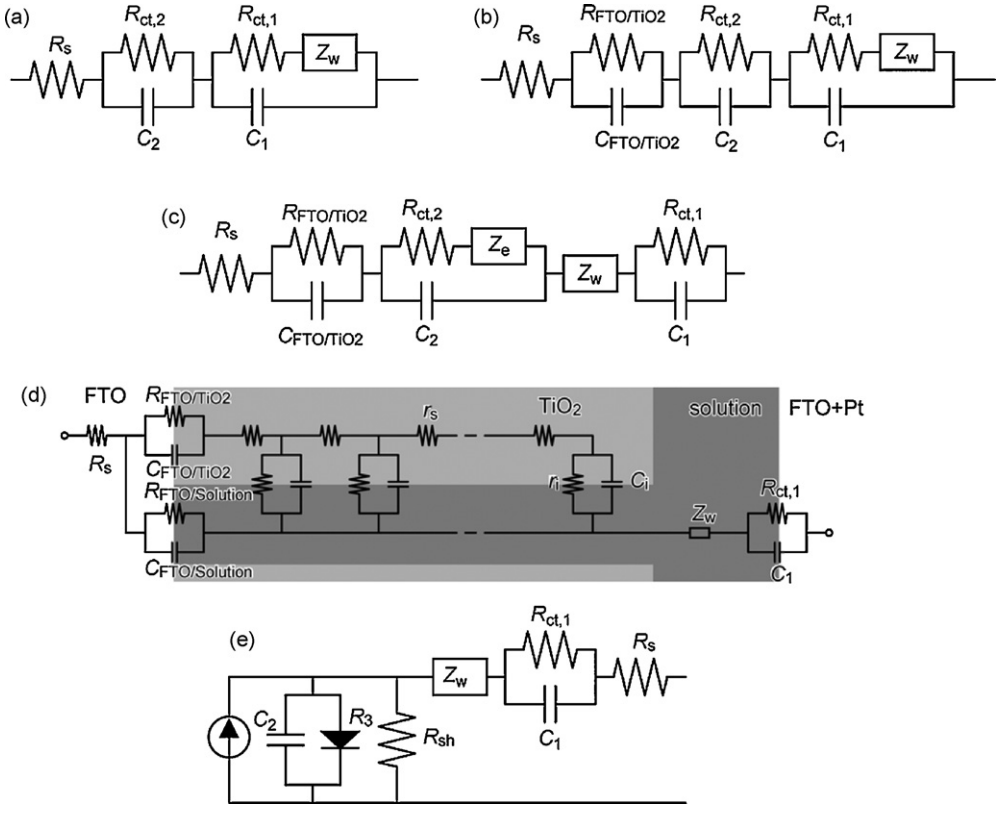

Fig. 1. Equivalent circuits of DSC reported previously.

calculate the conversion efficiency of the theoretical DSC. Tanaka [106] applied the theoretical model proposed by Ferber et al. [105] to the investigation of a TiO_2/organic dye/organic hole-conductor type DSC. Meanwhile, these models have not been extended to the impedance simulation.

In the present study, we introduced a theoretical model for EIS and *I–V* curve simulations. We derived the equations of Faradaic impedance of a photoelectrode and a counter electrode. In addition, the simulations of cell impedance and *I–V* curve of the DSC were also performed testing the new theories proposed in the present paper.

2. Theory

The present model of the DSC is composed of three parts as follows:

(a) Photoelectrode (anode) which consists of a TiO_2 semiconductor film with adsorbed dye on the fluorine-doped SnO_2 (FTO) substrate.
(b) Electrolyte solution containing I^- and I_3^-.
(c) Counter electrode (cathode).

2.1. Theoretical model of photoelectrode

Fig. 2 shows the theoretical model of the photoelectrode. The horizontal solid line in the TiO_2 film represents the conduction band energy level. Schottky barrier is formed at the TiO_2 film/electrolyte solution interface. The space charge layer of the thickness W is formed in the TiO_2 film at electrolyte side. Potential gradient (band bending) exists in the space charge layer. The potential of the photoelectrode E_a is defined as the conduction band energy level in the semiconductor bulk. E_{fb} is the flat band potential of the photoelectrode.

During the illumination of the photoelectrode, electrons in the dye are photoexcited from the highest occupied molecular orbital (HOMO) to the lowest unoccupied molecular orbital (LUMO). The excited electrons are injected into the conduction band of the TiO_2 film, and then migrate in the space charge layer by the electric field grandient. In this process, the dye is oxidized.

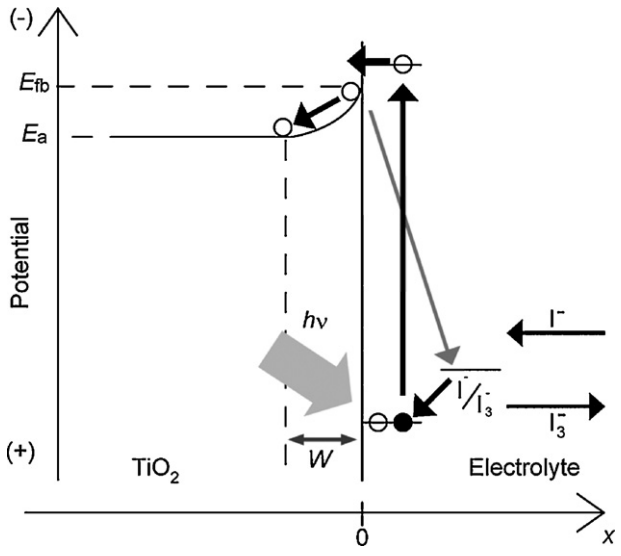

Fig. 2. Scheme to present the processes of photoelectrode.

The oxidized dye is reduced by the reaction with I^-. I^- is oxidized to I_3^- by the following reaction.

$$3I^- \rightarrow I_3^- + 2e^- \quad (1)$$

I_3^- diffuses to the bulk solution or reacts with electron injected into the TiO_2 film surface layer by the back electron transfer reaction in Eq. (2).

$$I_3^- + 2e^- \rightarrow 3I^- \quad (2)$$

2.2. Faradaic impedance of photoelectrode

Faradaic impedance is derived under following assumptions.

(A) Excitation and recombination of the electron do not occur in the semiconductor bulk.
(B) The chemicals excepting I_3^- do not react with the photoexcited electron on the TiO_2 film surface.
(C) The electron excitation rate depends on the light intensity and the oxidant/reductant ratio of the dye.
(D) The all electrons excited to LUMO are injected into the TiO_2 film surface layer.
(E) The potential difference between the redox potential of I^-/I_3^- and LUMO does not change.
(F) The redox potential of I^-/I_3^- and E_{fb} does not change in the alternating potential signal.
(G) No intermolecular interactions exist.

Firstly, the mass balance equations for four parameters are derived. The four parameters are as follows: the concentration of I^- on the photoelectrode ($c_{I^-,a}$ [mol cm^{-3}]), the concentration of I_3^- on the photoelectrode ($c_{I_3^-,a}$ [mol cm^{-3}]), the ratio of the oxidized dye (θ), and the electron density in the TiO_2 film surface layer (n_s [mol cm^{-3}]). In the present paper, the concentrations of I^- and I_3^- are used instead of the activities of them since intermolecular interactions are not considered in this model. It is noted that the value of the θ takes from 0 to 1.

The mass balance of $c_{I_3^-,a}$ is written as:

$$h_1 \frac{dc_{I_3^-,a}}{dt} = v_1 - v_2 - J_{I_3^-,a} = k_1 c_{I^-,a}^3 \theta^2 - k_2 n_s c_{I_3^-,a} - J_{I_3^-,a}, \quad (3)$$

where v_1 [mol cm^{-2} s^{-1}] is the rate of oxidation of I^- (Eq. (1)), v_2 [mol cm^{-2} s^{-1}] is the rate of reduction of I_3^- (Eq. (2)), $J_{I_3^-,a}$ [mol cm^{-2} s^{-1}] is the flux of I_3^-, k_1 [cm^7 mol^{-2} s^{-1}] is the rate constant of the oxidation of I^- and k_2 [cm^4 mol^{-1} s^{-1}] is the rate constant of the reduction of I_3^-. The k_1 and k_2 are normally potential-dependent rate constants in a Faradaic impedance simulation because these reactions are electrochemical processes. However, the k_1 and k_2 can be dealt with potential-independent rate constant in this study since it is assumed that the redox potential of I^-/I_3^- and E_{fb} take constant values. In addition, h_1 is the thickness of the reaction layer of the electrochemical reactions in Eqs. (1) and (2) on the photoelectrode.

The mass balance of $c_{I^-,a}$ is written as:

$$h_1 \frac{dc_{I^-,a}}{dt} = -3v_1 + 3v_2 - J_{I^-,a} = -3k_1 c_{I^-,a}^3 \theta^2 + 3k_2 n_s c_{I_3^-,a} - J_{I^-,a}, \quad (4)$$

where $J_{I^-,a}$ [mol cm^{-2} s^{-1}] is the flux of the I^-.

The ratio of oxidized dye θ increases with the light illumination and decreases with the oxidation of I^- in Eq. (1). The mass balance of θ is described as:

$$n_0 \frac{d\theta}{dt} = G - 2v_1 = (1-\theta)G_0 - 2k_1 c_{I^-,a}^3 \theta^2, \quad (5)$$

where n_0 [mol cm^{-2}] is surface concentration of the adsorbed dye. G [mol cm^{-2} s^{-1}] is the electron excitation rate under light illu-

mination to the photoelectrode. G_0 [mol cm^{-2} s^{-1}] is defined as the electron excitation rate under light illumination without the oxidized dye ($\theta = 0$).

The n_s increases with the increase of the excited electron by the light illumination. The n_s decreases with the back electron transfer reaction and migration to the TiO_2 bulk. Therefore, the mass balance of n_s is represented as:

$$h_2 \frac{dn_s}{dt} = G - 2v_2 - (\text{migration rate}) = (1-\theta)G_0 - 2k_2 n_s c_{I_3^-,a} - n_s \mu \vec{E}, \quad (6)$$

where h_2 [cm] is the thickness of TiO_2 film surface layer, μ [cm^2 V^{-1} s^{-1}] is the electron mobility in the TiO_2 film and $\vec{E}$ is the electric field in the space charge layer.

The electric field $\vec{E}$ is represented as (see Appendix A):

$$\vec{E} = \sqrt{\frac{2qN_D(E_a - E_{fb})}{\kappa_s}}, \quad (7)$$

where q [C] is the elementary charge, N_D [cm^{-3}] is the donor density and κ_s [F cm^{-1}] is the dielectric constant.

From Eqs. (4)–(7), the mass balances of c_{I^-}, $c_{I_3^-}$, θ and n_s at the steady-state are represented by Eqs. (8)–(11). The steady-state of c_{I^-}, $c_{I_3^-}$, θ and n_s are symbolized as $\bar{c}_{I_3^-,a}$, $\bar{c}_{I^-,a}$, $\bar{\theta}$ and $\bar{n}_s$. The $J_{I^-,a}$ and $J_{I_3^-,a}$ obey the Fick's first law.

$$-3k_1 \bar{c}^3_{I^-,a}\bar{\theta}^2 + 3k_2 \bar{n}_s \bar{c}_{I_3^-,a} + \frac{D_{I^-}(c^*_{I^-,a} - \bar{c}_{I^-,a})}{\delta_a} = 0 \quad (8)$$

$$k_1 \bar{c}^3_{I^-,a}\bar{\theta}^2 - k_2 \bar{n}_s \bar{c}_{I_3^-,a} + \frac{D_{I_3^-}(c^*_{I_3^-,a} - \bar{c}_{I_3^-,a})}{\delta_a} = 0 \quad (9)$$

$$(1-\bar{\theta})G_0 - 2k_1 \bar{c}^3_{I^-,a}\bar{\theta}^2 = 0 \quad (10)$$

$$(1-\bar{\theta})G_0 - 2k_2 \bar{n}_s \bar{c}_{I_3^-,a} - \bar{n}_s \mu \sqrt{\frac{2qN_D(E_a - E_{fb})}{\kappa_s}} = 0 \quad (11)$$

In Eqs. (8) and (9), D_{I^-} [cm^2 s^{-1}] and $D_{I_3^-}$ [cm^2 s^{-1}] are diffusion coefficients of the I^- and I_3^-, respectively, $c^*_{I^-,a}$ and $c^*_{I_3^-,a}$ are the bulk concentrations of I^- and I_3^-, respectively.

By the transformations of Eqs. (8)–(11), it is found that the relations of the $\bar{c}_{I_3^-,a}$, $\bar{c}_{I^-,a}$, $\bar{\theta}$ and $\bar{n}_s$ are correlated by the seventh order equations. In this case, the accurate values of $\bar{c}_{I_3^-,a}$, $\bar{c}_{I^-,a}$, $\bar{\theta}$ and $\bar{n}_s$ could not be calculated since the no formula exists to resolve the seventh order equations according to Abel-Ruffuni's theorem [107]. In this study, the approximate values of $\bar{c}_{I_3^-,a}$, $\bar{c}_{I^-,a}$, $\bar{\theta}$ and $\bar{n}_s$ are estimated by using the Newton–Raphson method (see Appendix B) [108].

The charge balance of the photoelectrode is considered. The current density I of the photoelectrode is proportionate to the flux of the electrons which migrate in the space charge layer (Eq. (12)) [109].

$$I = Fn_s \mu \vec{E} \quad (12)$$

In Eq. (12), F [C mol^{-1}] is the Faraday constant.

The following equation is derived from Eq. (12) by Talyor series expansion with neglecting higher order terms than second order one.

$$\Delta I = F\mu \left(\sqrt{\frac{2qN_D(E_a - E_{fb})}{\kappa_s}} \Delta n_s + \frac{\bar{n}_s}{2} \sqrt{\frac{2qN_D}{\kappa_s(E_a - E_{fb})}} \Delta E_a \right) \quad (13)$$

Moreover, the Faradaic impedance $Z_{F,a}$ is determined by dividing both sides of Eq. (13) by the variation of the photoelectrode potential ΔE_a.

$$\frac{1}{Z_{F,a}} = \frac{\Delta I}{\Delta E_a} = F\mu \left(\sqrt{\frac{2qN_D(E_a - E_{fb})}{\kappa_s}} \frac{\Delta n_s}{\Delta E_a} + \frac{\bar{n}_s}{2} \sqrt{\frac{2qN_D}{\kappa_s(E_a - E_{fb})}} \right) \quad (14)$$

From Eq. (14), $Z_{F,a}$ is obtained as a function of $\Delta n_s/\Delta E_a$ which can be derived as following processes.

Eq. (15) is derived from Eq. (3) by Taylor series expansion.

$$h_1 \frac{d\Delta c_{I^-,a}}{dt} = -6k_1 \bar{c}^3_{I^-,a}\bar{\theta}\Delta\theta - 9k_1 \bar{c}^2_{I^-,a}\bar{\theta}^2 \Delta c_{I^-,a} + 3k_2 \bar{c}_{I_3^-,a}\Delta n_s + 3k_2 \bar{n}_s \Delta c_{I_3^-,a} - \Delta J_{I^-,a} \quad (15)$$

Eq. (16) can be obtained from Eq. (15) by Fourier transformation and dividing both sides of Eq. (15) by ΔE_a.

$$\left(j\omega h_1 + 9k_1 \bar{c}^2_{I^-,a}\bar{\theta}^2 + \frac{\Delta J_{I^-,a}}{\Delta c_{I^-,a}} \right) \frac{\Delta c_{I^-,a}}{\Delta E_a} = -6k_1 \bar{c}^3_{I^-,a}\bar{\theta}\frac{\Delta\theta}{\Delta E_a} + 3k_2 \bar{c}_{I_3^-,a}\frac{\Delta n_s}{\Delta E_a} + 3k_2 \bar{n}_s \frac{\Delta c_{I_3^-,a}}{\Delta E_a} \quad (16)$$

In Eq. (16), j is the unit of imaginary number and ω is the angular frequency.

Moreover, the following equations are derived from Eqs. (4)–(6) by same calculation procedure.

$$\left(j\omega h_1 + k_2 \bar{n}_s + \frac{\Delta J_{I_3^-,a}}{\Delta c_{I_3^-,a}} \right) \frac{\Delta c_{I_3^-,a}}{\Delta E_a} = 2k_1 \bar{c}^3_{I^-,a}\bar{\theta}\frac{\Delta\theta}{\Delta E_a} - k_2 \bar{c}_{I_3^-,a}\frac{\Delta n_s}{\Delta E_a} + 3k_1 \bar{c}^2_{I^-,a}\bar{\theta}^2 \frac{\Delta c_{I^-,a}}{\Delta E_a} \quad (17)$$

$$(j\omega n_0 + 4k_1 \bar{c}^3_{I_3^-,a}\bar{\theta} + G_0)\frac{\Delta\theta}{\Delta E_a} = -6k_1 \bar{c}^2_{I^-,a}\bar{\theta}^2 \frac{\Delta c_{I^-,a}}{\Delta E_a} \quad (18)$$

$$\left(j\omega h_2 + 2k_2 \bar{c}_{I_3^-,a} + \mu \sqrt{\frac{2qN_D(E_a - E_{fb})}{\kappa_s}} \right) \frac{\Delta n_s}{\Delta E_a} = -G_0 \frac{\Delta\theta}{\Delta E_a} - 2k_2 \bar{n}_s \frac{\Delta c_{I_3^-,a}}{\Delta E_a} - \frac{\mu \bar{n}_s}{2} \sqrt{\frac{2qN_D}{\kappa_s(E_a - E_{fb})}} \quad (19)$$

The diffusion of I^- from the bulk solution to the interface of electrode is governed by Fick's second law.

$$\frac{\partial c_{I^-,a}}{\partial t} = D_{I^-} \frac{\partial^2 c_{I^-,a}}{\partial x^2} \quad (20)$$

In Eq. (20), x is the distance from the electrode surface to the solution bulk. The following equation is derived from Eq. (20) by Taylor series expansion and Fourier transformation.

$$j\omega \Delta c_{I^-,a} = D_{I^-} \frac{\partial^2 \Delta c_{I^-,a}}{\partial x^2} \quad (21)$$

The general solution for Eq. (21) is:

$$\Delta c_{I^-,a} = K \exp\left\{ x \left(\frac{j\omega}{D_{I^-}} \right)^{1/2} \right\} + L \exp\left\{ -x \left(\frac{j\omega}{D_{I^-}} \right)^{1/2} \right\}, \quad (22)$$

where K and L are constants. Because the concentration of I^- is constant in the bulk of solution, the boundary condition is $\Delta c_{I^-,a} = 0$

at $x = \delta_a$, where δ_a represents the diffusion layer thickness. By substituting the boundary condition into Eq. (22), Eq. (23) is obtained.

$$K = -L \exp\left\{-2\delta_a\left(\frac{j\omega}{D_{I^-}}\right)^{1/2}\right\} \tag{23}$$

By substituting Eq. (23) into Eq. (22):

$$\Delta c_{I^-,a} = 2L(j\omega D_{I^-})^{1/2} \exp\left\{-\delta_a\left(\frac{j\omega}{D_{I^-}}\right)^{1/2}\right\} \sinh\left\{(x-\delta_a)\left(\frac{j\omega}{D_{I^-}}\right)^{1/2}\right\}, \tag{24}$$

is obtained. From Fick's first law,

$$\Delta J_{I^-,a} = -D_{I^-}\left|\frac{\partial \Delta c_{I^-,a}}{\partial x}\right|_{x=0} = 2L(j\omega D_{I^-})^{1/2} \exp\left\{-\delta_a\left(\frac{j\omega}{D_{I^-}}\right)^{1/2}\right\} \coth\left\{-\delta_a\left(\frac{j\omega}{D_{I^-}}\right)^{1/2}\right\} \tag{25}$$

The following relation is derived from Eqs. (24) and (25).

$$\frac{\Delta c_{I^-,a}}{\Delta J_{I^-,a}} = (j\omega D_{I^-})^{-1/2} \tanh\left\{\delta_a\left(\frac{j\omega}{D_{I^-}}\right)^{1/2}\right\} \tag{26}$$

The following equation is also derived by same calculation procedure.

$$\frac{\Delta c_{I_3^-,a}}{\Delta J_{I_3^-,a}} = (j\omega D_{I_3^-})^{-1/2} \tanh\left\{\delta_a\left(\frac{j\omega}{D_{I_3^-}}\right)^{1/2}\right\} \tag{27}$$

The $\Delta n_s/\Delta E_a$ is obtained as follows.

$$\frac{\Delta n_s}{\Delta E_a} = \frac{W_1}{W_2} \tag{28}$$

In Eq. (28), W_1 and W_2 are represented by the following equations.

$$W_1 = \left(4k_1\bar{c}_{I^-,a}^3\bar{\theta}W_3W_4 + (G_0 + j\omega n_0)\left(9k_1\bar{c}_{I^-,a}^2\bar{\theta}^2\left(\frac{\Delta J_{I_3^-,a}}{\Delta c_{I_3^-,a}} + j\omega h_1\right) + W_3W_4\right)\right)\frac{\mu\bar{n}_s}{2}\sqrt{\frac{2qN_D}{\kappa_s(E_a - E_{fb})}} \tag{29}$$

$$W_2 = -4k_1\bar{c}_{I^-,a}^3\bar{\theta}W_3\left(W_5 + \frac{\Delta J_{I_3^-,a}}{\Delta c_{I_3^-,a}}W_6 + j\omega W_7\right) - G_0\left(9k_1\bar{c}_{I^-,a}^2\bar{\theta}^2\left(\frac{\Delta J_{I_3^-,a}}{\Delta c_{I_3^-,a}} + j\omega h_1\right)\left(\mu\sqrt{\frac{2qN_D(E_a - E_{fb})}{\kappa_s}} + j\omega h_2\right) + W_3\left(W_5 + \frac{\Delta J_{I_3^-,a}}{\Delta c_{I_3^-,a}}W_6 + j\omega W_7\right)\right) - j\omega n_0\left(9k_1\bar{c}_{I^-,a}^2\bar{\theta}^2W_6\left(\frac{\Delta J_{I_3^-,a}}{\Delta c_{I_3^-,a}} + j\omega h_1\right) + W_3\left(W_5 + \frac{\Delta J_{I_3^-,a}}{\Delta c_{I_3^-,a}}W_6 + j\omega W_7\right)\right) \tag{30}$$

In Eqs. (29) and (30), W_3–W_7 are:

$$W_3 = \frac{\Delta J_{I^-,a}}{\Delta c_{I^-,a}} + j\omega h_1, \tag{31}$$

$$W_4 = \frac{\Delta J_{I_3^-,a}}{\Delta c_{I_3^-,a}} + k_2\bar{n}_s + j\omega h_1, \tag{32}$$

$$W_5 = \mu\sqrt{\frac{2qN_D(E_a - E_{fb})}{\kappa_s}}(k_2\bar{n}_s + j\omega h_1), \tag{33}$$

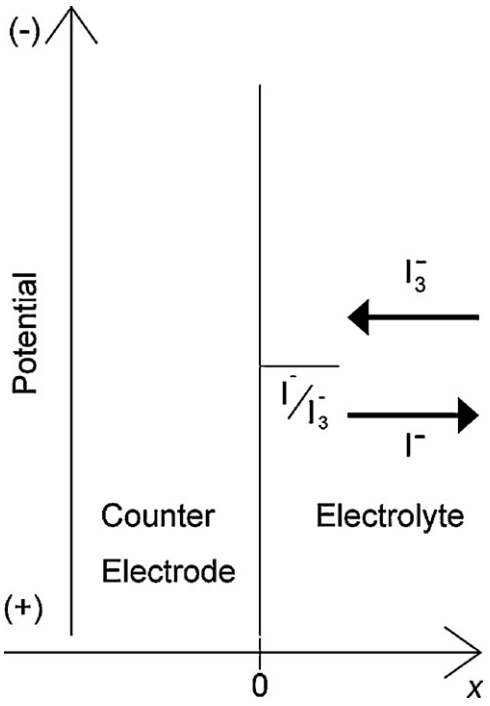

Fig. 3. Scheme to present the processes of counter electrode.

$$W_6 = \mu\sqrt{\frac{2qN_D(E_a - E_{fb})}{\kappa_s}} + 2k_2\bar{c}_{I_3^-,a} + j\omega h_2, \tag{34}$$

$$W_7 = 2k_2h_1\bar{c}_{I_3^-,a} + k_2h_2\bar{n}_s + j\omega h_1h_2. \tag{35}$$

2.3. The model of counter electrode

Fig. 3 shows the theoretical model of the counter electrode. Although the some mechanisms for the redox reaction of I^-/I_3^- have been proposed for platinum and carbon counter electrodes [69,78,110,111], the reactions in Eqs. (1) and (2) are used for the calculation of the Faradaic impedance in the present study.

2.4. Faradaic Impedance of counter electrode

The mass balances of the concentrations of I^- ($c_{I^-,c}$) and I_3^- ($c_{I_3^-,c}$) on the counter electrode are as follows.

$$h_3\frac{dc_{I^-,c}}{dt} = 3k_3c_{I_3^-,c} - 3k_{-3}c_{I^-,c}^3 - J_{I^-,c} \tag{36}$$

$$h_3\frac{dc_{I_3^-,c}}{dt} = -k_3c_{I_3^-,c} + k_{-3}c_{I^-,c}^3 - J_{I_3^-,c} \tag{37}$$

The h_3 is the reacition layer thickness on the counter electrode and the k_3 [cm s^{-1}] and k_{-3} [cm^7 mol^{-2} s^{-1}] are potential-dependent rate constants ($k_i = k_i' \exp(b_iE_c)$) [112], where E_c is the

potential of the counter electrode, k_i' is the rate constant at $E_c = 0$ and b_i is the Tafel constant.

Since $dc_{I^-,c}/dt = 0$ and $dc_{I_3^-,c}/dt = 0$ at the steady-state, the mass balances at the steady-state are represented as follows:

$$3k_3\bar{c}_{I_3^-,c} - 3k_{-3}\bar{c}_{I^-,c}^3 + \frac{D_{I^-}(c_{I^-,c}^* - \bar{c}_{I^-,c})}{\delta_c} = 0, \tag{38}$$

$$-k_3\bar{c}_{I_3^-,c} + k_{-3}\bar{c}_{I^-,c}^3 + \frac{D_{I_3^-}(c_{I_3^-,c}^* - \bar{c}_{I_3^-,c})}{\delta_c} = 0, \tag{39}$$

where $\bar{c}_{I_3^-,c}$, $\bar{c}_{I^-,c}$ are the concentrations of I^- and I_3^-, respectively, on the counter electrode at the steady-state. From Eqs. (38) and (39), $\bar{c}_{I_3^-,c}$ and $\bar{c}_{I^-,c}$ are calculated as follows.

$$\bar{c}_{I^-,c} = \frac{-2k_{-3}(D_{I_3^-}/\delta_c)^2(D_{I^-}/\delta_c) - 2k_3k_{-3}(D_{I_3^-}/\delta_c)(D_{I^-}/\delta_c) + 2^{1/3}(B_1+B_2)^{2/3}}{3\times 2^{2/3}k_{-3}(D_{I_3^-}/\delta_c)(B_1+B_2)^{1/3}} \tag{40}$$

$$\bar{c}_{I_3^-,c} = \frac{2\times 2^{1/3}(k_{-3}(D_{I_3^-}/\delta_c)^2(D_{I^-}/\delta_c)^2 + k_3k_{-3}(D_{I_3^-}/\delta_c)(D_{I^-}/\delta_c)^2)}{18(D_{I_3^-}/\delta_c)^2k_{-3}(B_1+B_2)^{1/3}} + \frac{(18k_{-3}c_{I_3^-,c}^*(D_{I_3^-}/\delta_c)^2 + 6k_{-3}c_{I^-,c}^*(D_{I_3^-}/\delta_c)(D_{I^-}/\delta_c))(B_1+B_2)^{1/3}}{18(D_{I_3^-}/\delta_c)^2k_{-3}(B_1+B_2)^{1/3}} - \frac{2^{2/3}(D_{I^-}/\delta_c)(B_1+B_2)^{1/3}}{18(D_{I_3^-}/\delta_c)^2k_{-3}} \tag{41}$$

In Eqs. (40) and (41), B_1 and B_2 are represented as follows.

$$B_1 = 9k_{-3}^2c_{I^-,c}^*\left(\frac{D_{I_3^-}}{\delta_c}\right)^3\frac{D_{I^-}}{\delta_c} + 27k_3k_{-3}^2c_{I_3^-,c}^*\left(\frac{D_{I_3^-}}{\delta_c}\right)^3 + 9k_3k_{-3}^2c_{I^-,c}^*\left(\frac{D_{I_3^-}}{\delta_c}\right)^2\frac{D_{I^-}}{\delta_c} \tag{42}$$

$$B_2 = \sqrt{k_{-3}^3\left(\frac{D_{I_3^-}}{\delta_c}\right)^3\left(4\left(\frac{D_{I^-}}{\delta_c}\right)^3\left(\frac{D_{I_3^-}}{\delta_c}+k_3\right)^3 + 81\frac{D_{I_3^-}}{\delta_c}\left(3k_3c_{I_3^-,c}^*\frac{D_{I_3^-}}{\delta_c} + c_{I^-,c}^*\frac{D_{I^-}}{\delta_c}\left(\frac{D_{I_3^-}}{\delta_c}+k_3\right)\right)^2k_{-3}\right)} \tag{43}$$

The charge balance of the counter electrode is as below.

$$I = -2F(k_3c_{I_3^-,c} - k_{-3}c_{I^-,c}^3) \tag{44}$$

The following equation is derived from Eq. (44) by Taylor series expansion:

$$\Delta I = -2F(k_3\Delta c_{I_3^-,c} + b_3k_3\bar{c}_{I_3^-,c}\Delta E_c - 3k_{-3}\bar{c}_{I^-,c}^2\Delta c_{I^-,c} - b_{-3}k_{-3}\bar{c}_{I^-,c}^3\Delta E_c), \tag{45}$$

where b_3 and b_{-3} are the Tafel constants of k_3 and k_{-3}, respectively.

The Faradaic impedance $Z_{F,c}$ is obtained from the reciprocal of the admittance $\Delta I/\Delta E_c$ from Eq. (45).

$$\frac{1}{Z_{F,c}} = \frac{\Delta I}{\Delta E_c} = -2F\left(k_3\frac{\Delta c_{I_3^-,c}}{\Delta E_c} + b_3k_3\bar{c}_{I_3^-,c} - 3k_{-3}\bar{c}_{I^-,c}^2\frac{\Delta c_{I^-,c}}{\Delta E_c} - b_{-3}k_{-3}\bar{c}_{I^-,c}^3\right) \tag{46}$$

The following equations are derived from Eqs. (36) and (37) by Fourier transformation and Taylor series expansion.

$$\left(j\omega h_3 + 9k_{-3}\bar{c}_{I^-,c}^2 + \frac{\Delta J_{I^-,c}}{\Delta c_{I^-,c}}\right)\frac{\Delta c_{I^-,c}}{\Delta E_c} = 3k_3\frac{\Delta c_{I_3^-,c}}{\Delta E_c} - 3b_{-3}k_{-3}\bar{c}_{I^-,c}^3 + 3b_3k_3\bar{c}_{I_3^-,c} \tag{47}$$

$$\left(j\omega h_3 + k_3 + \frac{\Delta J_{I_3^-,c}}{\Delta c_{I_3^-,c}}\right)\frac{\Delta c_{I_3^-,c}}{\Delta E_c} = 3k_{-3}\bar{c}_{I^-,c}^2\frac{\Delta c_{I^-,c}}{\Delta E_c} + b_{-3}k_{-3}\bar{c}_{I^-,c}^3 - b_3k_3\bar{c}_{I_3^-,c} \tag{48}$$

In addition, the $\Delta J_{I^-,c}/\Delta c_{I^-,c}$ and $\Delta J_{I_3^-,c}/\Delta c_{I^-,c}$ are calculated as follows.

$$\frac{\Delta J_{I^-,c}}{\Delta c_{I^-,c}} = -(j\omega D_{I^-})^{1/2}\coth\left\{-\delta_c\left(\frac{j\omega}{D_{I^-}}\right)^{1/2}\right\} \tag{49}$$

$$\frac{\Delta J_{I_3^-,c}}{\Delta c_{I_3^-,c}} = -(j\omega D_{I_3^-})^{1/2}\coth\left\{-\delta_c\left(\frac{j\omega}{D_{I_3^-}}\right)^{1/2}\right\} \tag{50}$$

From Eqs. (47)–(50), $\Delta c_{I^-,c}/\Delta E_c$ and $\Delta c_{I_3^-,c}/\Delta E_c$ are derived as follows.

$$\frac{\Delta c_{I^-,c}}{\Delta E_c} = \frac{3(k_3b_3\bar{c}_{I_3^-,c} - k_{-3}b_{-3}\bar{c}_{I^-,c}^3)(\omega h_3 - j(\Delta J_{I_3^-,c}/\Delta c_{I_3^-,c}))}{j\omega^2h_3^2 + \omega h_3(k_3 + 9k_{-3}\bar{c}_{I^-,c}^2 + (\Delta J_{I^-,c}/\Delta c_{I^-,c}) + (\Delta J_{I_3^-,c}/\Delta c_{I_3^-,c})) - j(9k_{-3}\bar{c}_{I^-,c}^2(\Delta J_{I_3^-,c}/\Delta c_{I_3^-,c}) + (k_3 + (\Delta J_{I_3^-,c}/\Delta c_{I_3^-,c}))(\Delta J_{I^-,c}/\Delta c_{I^-,c}))} \tag{51}$$

$$\frac{\Delta c_{I_3^-}}{\Delta E_c} = \frac{(k_3b_3\bar{c}_{I_3^-,c} - k_{-3}b_{-3}\bar{c}_{I^-,c}^3)(\omega h_3 - j(\Delta J_{I^-,c}/\Delta c_{I^-,c}))}{j\omega^2h_3^2 + \omega h_3(k_3 + 9k_{-3}\bar{c}_{I^-,c}^2 + (\Delta J_{I^-,c}/\Delta c_{I^-,c}) + (\Delta J_{I_3^-,c}/\Delta c_{I_3^-,c})) - j(9k_{-3}\bar{c}_{I^-,c}^2(\Delta J_{I_3^-,c}/\Delta c_{I_3^-,c}) + (k_3 + (\Delta J_{I_3^-,c}/\Delta c_{I_3^-,c}))(\Delta J_{I^-,c}/\Delta c_{I^-,c}))} \tag{52}$$

The $Z_{F,c}$ are calculated by substituting Eqs. (51) and (52) into Eq. (46).

2.5. Simulation method

The calculations were performed by mathematical software Mathematica (Wolfram Research) and Excel 2007 (Microsoft Corporation). The impedance was calculated at 10 frequencies per decade in the frequency range from 1 mHz to 100 kHz. It is noted that the impedance above 100 kHz was not calculated since the values at the computation processes was too large to be calculated by a personal computer. In addition, the impedance of DSC was measured below 100 kHz in the papers reported recently [8,9,12]. Therefore, the impedance above 100 kHz was not dealt with in the present paper.

3. Results and discussion

3.1. Faradaic Impedance and I–E_a curve of photoelectrode

Faradaic impedance of the photoelectrode ($Z_{F,a}$) was calculated with Eqs. (14) and (28). In addition, the polarization curve (I–E_a curve) of the photoelectrode was simulated with Eq. (12).

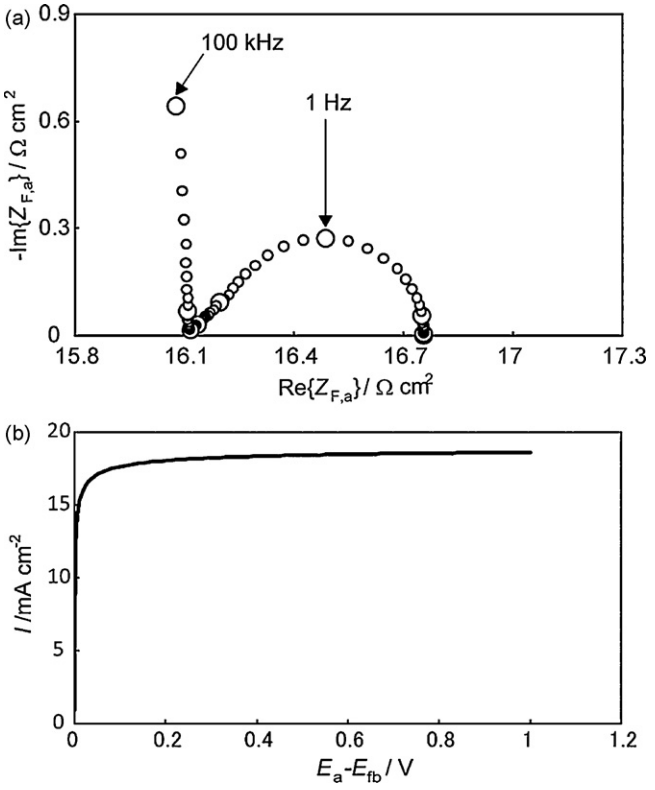

Fig. 4. (a) Nyquist plot of Faradaic impedance and (b) I–E_a curve of the photoelectrode calculated with the parameters in Table 1.

Fig. 4 shows the $Z_{F,a}$ and I–E_a curve calculated with the parameters in Table 1. Since it is assumed that the E_{fb} is 0 V, the potential of the photoelectrode is equal to E_a. Faradaic impedance cannot be calculated with Eq. (14) at $E_a = E_{fb}$ since the term $\tilde{n}_s/2(\sqrt{2qN_D/\kappa_s(E_a - E_{fb})})$ in right side in Eq. (14) becomes infinity. Therefore, the DC potential is set at 0.02 V for the Faradaic impedance simulation in this section. The Faradaic impedance at 0.02 V shown in Fig. 4(a) describes a part of semicircle in the high frequency range and locus of the finite diffusion impedance in the low frequency range. The finite diffusion impedance may be related to the diffusions of I_3^- and I^- and its locus shows straight line of 45 degrees to real axis in the high frequency range and converges on real axis in the low frequency range. In I–E_a curve shown in Fig. 4(b), the current drastically increases with the increase E_a between 0 and 0.05 V. On the other hand, the current takes constant value approximately at higher potential than 0.05 V. This shape of the I–E_a curve shown in Fig. 4(b) is similar to the typical current–potential curves of the photoelectrode used for DSC [113,114]. The current depends on the migration rate of the electrons in the space charge layer in the low potential region. Since the migration rate is proportionate to the slope of the Schottky barrier, the current increases with the increase of E_a in the low potential region. By contrast, the migration rate is faster than the electron excitation rate $(1-\theta)G_0$, the charge transfer rate ν_1 and fluxes of I^- and I_3^-, J_{I^-} and $J_{I_3^-}$, in the high potential region. In addition, the electron density in the TiO_2 film surface layer n_s in the high potential region is smaller than that in the low potential region. The values of n_s at 0.001 and 0.5 V, calculated by Newton–Raphson method, were 6.90×10^{-8} and 5.19×10^{-9} mol cm^{-3}, respectively. The decrease of the n_s results in the decrease of the back electron transfer reaction rate. In this case, the current depends on the $(1-\theta)G_0$, ν_1, J_{I^-} and $J_{I_3^-}$ which are potential-independent parameters. Therefore, the current takes almost constant values in the high potential region.

Table 1
The parameters list to calculate Faradaic impedance and I–E_a curve of the photoelectrode in Fig. 4.

Parameter	Value	Ref.
κ_s [F cm^{-1}]	4.43×10^{-12}	
D_{I^-} [cm^2 s^{-1}]	10^{-5}	[25]
$D_{I_3^-}$ [cm^2 s^{-1}]	10^{-5}	[25]
T [K]	300	
$c^*_{I^-,a}$ [mol cm^{-3}]	5×10^{-4}	
$c^*_{I_3^-,a}$ [mol cm^{-3}]	5×10^{-5}	
G_0 [mol cm^{-2} s^{-1}]	2×10^{-7}	
D_e [cm^2 s^{-1}]	5×10^{-5}	[105]
k_1 [cm^7 mol^{-2} s^{-1}]	10^7	
k_2 [cm^4 mol^{-1} s^{-1}]	10^4	
N_D [cm^{-3}]	10^{16}	
δ_a [cm]	0.002	
n_0 [mol cm^{-2}]	10^{-8}	
h_1,h_2 [cm]	10^{-7}	

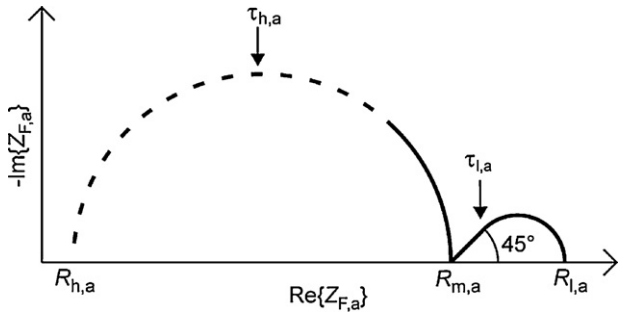

Fig. 5. The schematic illustration of Faradaic impedance spectrum of the photoelectrode.

Next the authors discuss the Faradaic impedance spectrum of the photoelectrode shown in Fig. 4(a). Fig. 5 shows the schematic illustration of typical Faradaic impedance spectrum of the photoelectrode. The Faradaic impedance, whose locus is semicircle, in the high frequency range is related to in the multiple electron transfer processes including photoexcitation, charge transfer between I^- and the dye, electron migration in the space charge layer and back electron transfer. The Faradaic impedance at the high frequency limit $R_{h,a}$ can be calculated from Eq. (14) (see Appendix C).

$$R_{h,a} = \frac{2}{F\mu\tilde{n}_s}\sqrt{\frac{\kappa_s(E_a - E_{fb})}{2qN_D}} \tag{53}$$

A resistance of the intersection point on the real axis in the middle frequency range $R_{m,a}$ is calculated as below (see Appendix C).

$$R_{m,a} = \frac{2}{F\mu\tilde{n}_s}\sqrt{\frac{\kappa_s(E_a - E_{fb})}{2qN_D}} + \frac{E_a - E_{fb}}{Fk_2\bar{c}_{I_3^-,a}\tilde{n}_s} \tag{54}$$

The $R_{m,a}$ depends on the parameters related to the multiple electron transfer processes. The diameter of the semicircle in the high frequency range can be determined as $E_a - E_{fb}/Fk_2\bar{c}_{I_3^-,a}\tilde{n}_s$ by subtracting $R_{h,a}$ from $R_{m,a}$. The time constant of the semicircle in high frequency range ($\tau_{h,a}$, in Fig. 5) is represented as below (see Appendix C).

$$\tau_{h,a} = \frac{h_2}{2k_2\bar{c}_{I_3^-,a}} \tag{55}$$

The locus of the impedance in the low frequency range is the feature of finite diffusion processes of I^- and I_3^-. The resistance at the low frequency limit $R_{l,a}$ is represented as below.

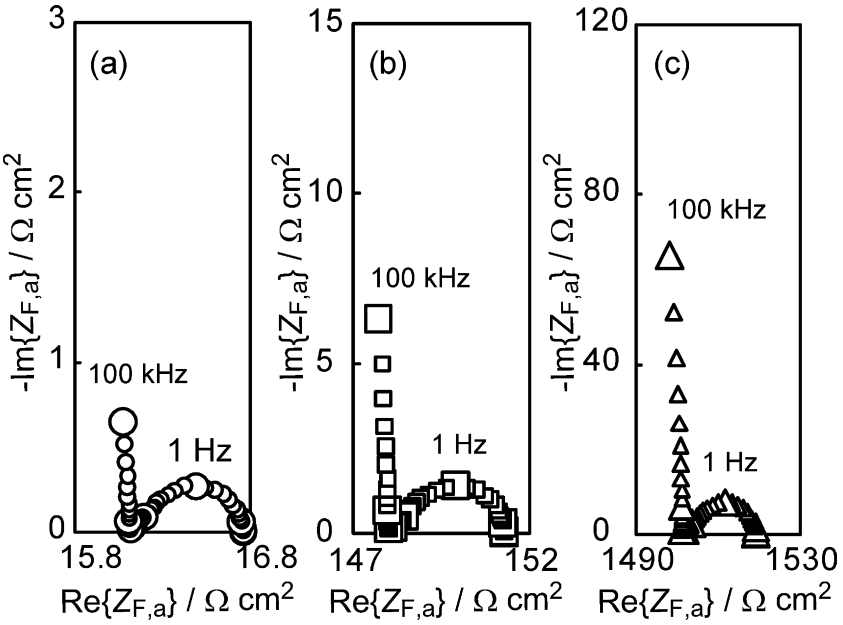

Fig. 6. Calculated results of Faradaic impedance of photoelectrode at various E_a (circle: 0.02 V; square: 0.1 V; triangle: 0.5 V). The parameter values for the calculations are written in Table 1.

$$R_{l,a} = \frac{2}{F\mu\bar{n}_s}\sqrt{\frac{\kappa_s(E_a - E_{fb})}{2qN_D}} + \frac{E_a - E_{fb}}{Fk_2\bar{c}_{I_3^-,a}\bar{n}_s} + \frac{9k_1\bar{c}^2_{I^-,a}\bar{\theta}^2\delta_a G_0(E_a - E_{fb})}{Fk_2\bar{c}_{I_3^-,a}D_{I^-}\bar{n}_s(G_0 + 4k_1\bar{c}^3_{I^-,a}\bar{\theta})} + \frac{\bar{n}_s\delta_a(E_a - E_{fb})}{F\bar{c}_{I_3^-,a}D_{I_3^-}\bar{n}_s} \quad (56)$$

The diffusion resistance $R_{diff,a}$ is defined as follows.

$$R_{diff,a} = R_{l,a} - R_{m,a} \quad (57)$$

The time constant of the finite diffusion impedance $\tau_{l,a}$ is described by following equation [115].

$$\tau_{l,a} = \frac{(\delta_a)^2}{D_{I_3^-}} \quad (58)$$

3.2. Effects of some parameters on the locus of Faradaic impedance of photoelectrode

Faradaic impedance of the photoelectrode is discussed with changing in the following parameters, E_a, D_{I^-}, $D_{I_3^-}$, k_2 and G_0. The other parameters are shown in Table 1.

The calculated results of $Z_{F,a}$ at various E_a are shown in Fig. 6. The $R_{m,a}$ increases with E_a and this tendency is in good agreement with Eq. (54). The $R_{diff,a}$ also increases with E_a, indicating that the contribution of diffusion rate becomes significant since the interfacial reactions are accelerated by the polarization.

Fig. 7(a) shows the $R_{m,a}$ calculated with Eq. (54) with the variations of $D_{I_3^-}$ and D_{I^-}. The $R_{m,a}$ increases with the increase of $D_{I_3^-}$ though the $R_{m,a}$ takes almost constant value with the variation of D_{I^-}. Fig. 7(b) shows the $R_{diff,a}$ calculated with Eq. (57) with the variations of $D_{I_3^-}$ and D_{I^-}. The $R_{diff,a}$ decreases with the increases of both $D_{I_3^-}$ and D_{I^-}, and the slope of decrease is large in the case of the increase of $D_{I_3^-}$. Meanwhile, the change in the $R_{diff,a}$ is very small with the variation of $D_{I_3^-}$. In general, the initial concentration of I^- is higher than that of I_3^- in the DSC [25] since I_3^- causes the back electron transfer reaction. The authors set that $c^*_{I^-}$ is 10 times larger than $c^*_{I_3^-}$. In this case, the finite diffusion impedance is governed by $J_{I_3^-}$.

Fig. 8(a) shows the $R_{m,a}$ calculated with Eq. (54) with the variation of k_2. The $R_{m,a}$ decreases with the increase of k_2 in the range between 10^0 cm^4 mol^{-1} s^{-1} and 10^4 cm^4 mol^{-1} s^{-1}, and the tendency is in good agreement with the second term in right side of Eq. (54). Contrary to this, the $R_{m,a}$ increases with the increase of k_2 above 10^5 cm^4 mol^{-1} s^{-1}. Fig. 8(b) and (c) shows the $\bar{n}_s$ and $\bar{c}_{I_3^-,a}$

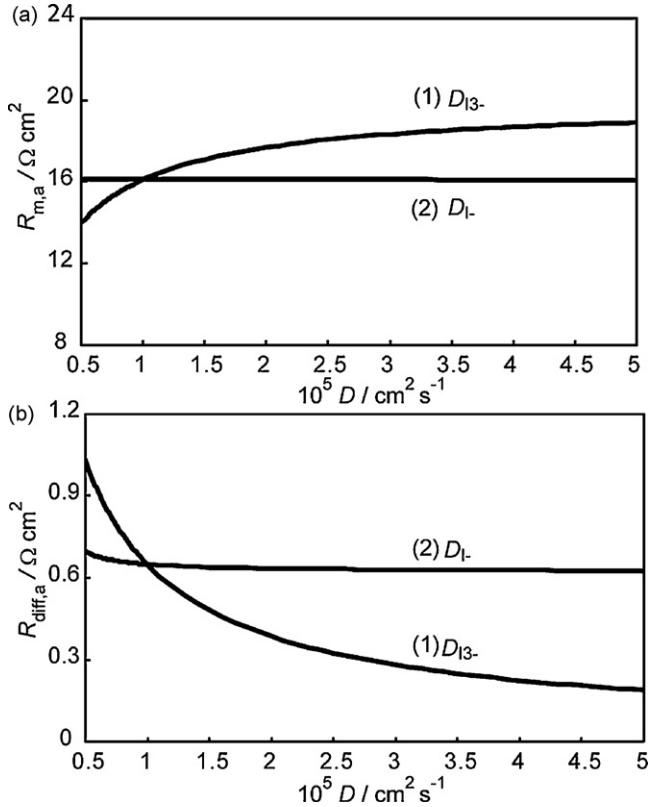

Fig. 7. Influences of diffusion coefficients on $R_{m,a}$ and $R_{diff,a}$. The curves indicated by (1) and (2) are the results with the variations of $D_{I_3^-}$ and D_{I^-}, respectively. The parameter values excepting $D_{I_3^-}$ and D_{I^-} for the calculations are written in Table 1.

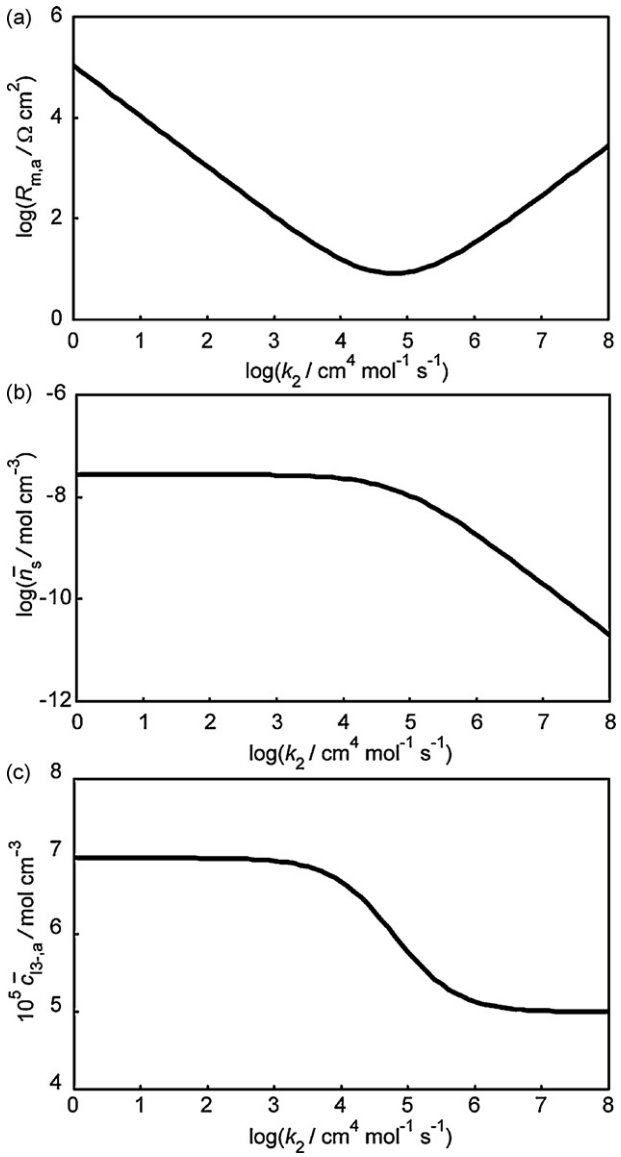

Fig. 8. Influence of k_2 on (a) $R_{m,a}$, (b) $\bar{n}_s$ and (c) $\bar{c}_{I_3^-,c}$. The parameter values excepting k_2 for the calculations are written in Table 1.

with the variation of the k_2. Because both $\bar{n}_s$ and $\bar{c}_{I_3^-,a}$ decrease with the k_2, the $R_{m,a}$ calculated with Eq. (54) increases with k_2 above 10^5 cm^4 mol^{-1} s^{-1}. These results indicate that the $R_{m,a}$ depends on the k_2 and take minimum value with the variation of the k_2.

Fig. 9 shows the $R_{m,a}$ and $R_{diff,a}$ calculated with Eqs. (54) and (57) with the variations of G_0. The $R_{m,a}$ decreases with G_0 below 10^{-6} mol cm^{-2} s^{-1} and takes almost constant value above 10^{-5} mol cm^{-2} s^{-1}. This result means that the interfacial reactions determine the total charge transfer rate of photoelectrode when G_0 takes relatively small value. On the other hand, $R_{diff,a}$ increases with G_0 above 10^{-5} mol cm^{-2} s^{-1}. This result indicates that the diffusion process determines the total rate in the case of high interfacial reaction rate.

3.3. Effects of some parameters on I–E_a curve of photoelectrode

The calculated results of I–E_a curves with the variation of G_0 are shown in Fig. 10. The current increases abruptly with E_a below about 0.05 V and becomes the limiting current region above about 0.05 V. The current becomes large depending on the value of G_0 in all potential regions. For example, the limiting current is about

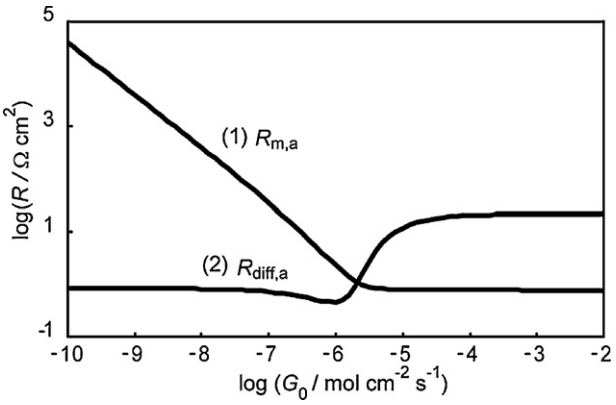

Fig. 9. Influence of G_0 on (1) $R_{m,a}$ and (2) $R_{diff,a}$. The parameter values excepting G_0 for the calculations are written in Table 1.

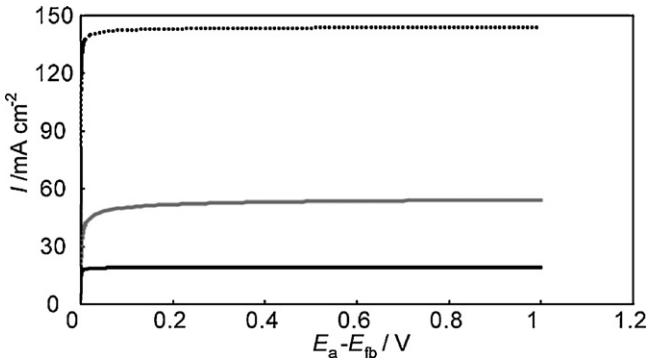

Fig. 10. Calculated results of I–E_a curves of photoelectrode with various G_0 (the solid line: 2×10^{-7} mol cm^{-2} s^{-1}, the gray line: 6×10^{-7} mol cm^{-2} s^{-1} and the dashed line: 2×10^{-5} mol cm^{-2} s^{-1}). The parameter values excepting G_0 for the calculations are written in Table 1.

140 mA cm^{-2} when $G_0 = 2 \times 10^{-5}$ mol cm^{-2} s^{-1}. This current value is equal to the diffusion limiting current of I^- estimated by the J_{I^-} at the steady-state ($= D_I(c^*_{I^-} - \bar{c}_{I^-})/\delta_a$). When the G_0 is sufficiently larger than $J_{I_3^-,a}$ and $J_{I^-,a}$, the I-E_a curves is governed by the diffusion of I^-. The calculated results of I–E_a curves with the variation of k_2 are shown in Fig. 11. The slope of current increase in the low potential region decreases with the increase of k_2. This result indicates that the back reaction inhibits the increase of I_3^- concentration on photoelectrode and electrode condition does not reach to the diffusion control.

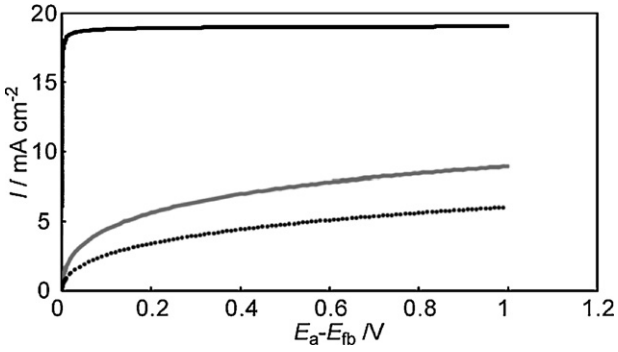

Fig. 11. Calculated results of I–E_a curves of photoelectrode with various k_2 (the solid line: 10^4 cm^4 mol^{-1} s^{-1}, the gray line: 5×10^5 cm^4 mol^{-1} s^{-1} and the dashed line: 10^6 cm^4 mol^{-1} s^{-1}). The parameter values excepting k_2 for the calculations are written in Table 1.

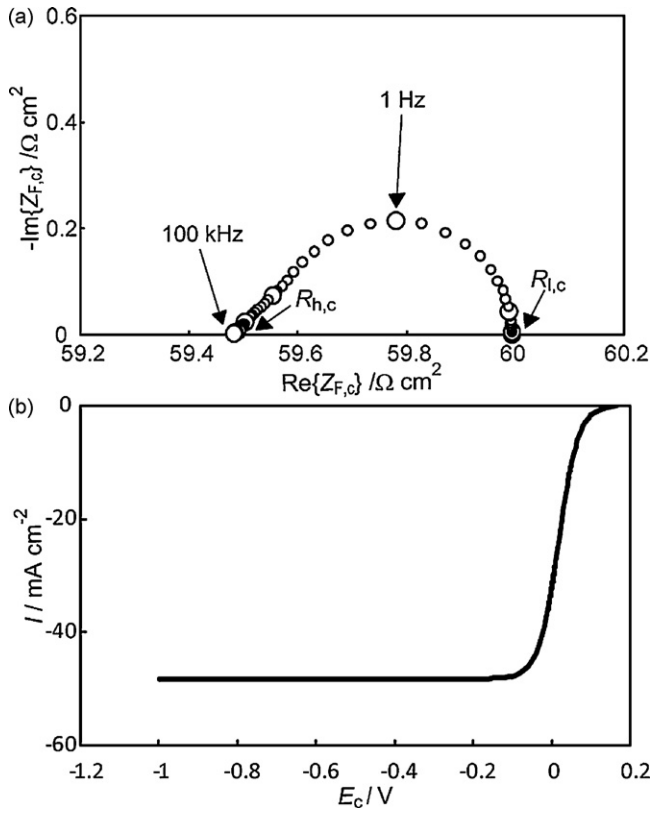

Fig. 12. (a) Nyquist plot of Faradaic impedance and (b) I–E_c curve of the counter electrode calculated with the parameters in Table 2.

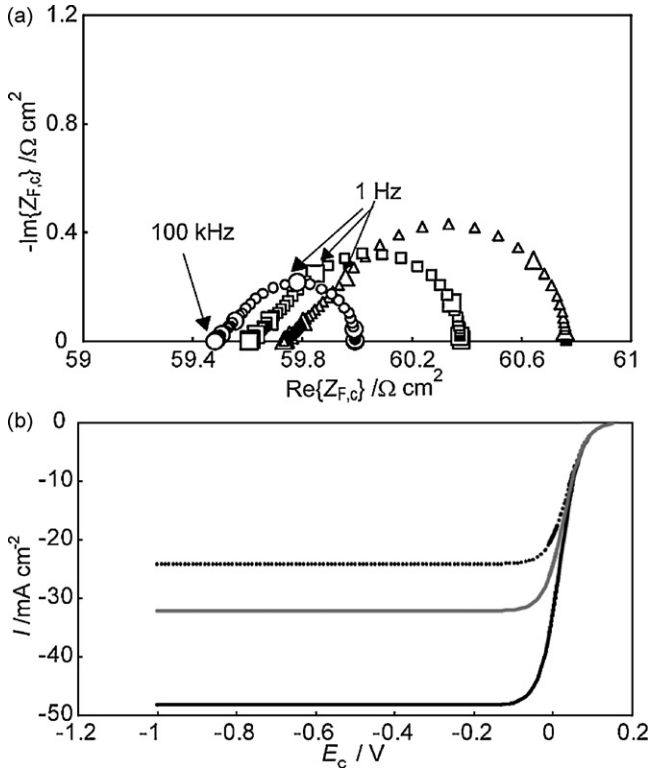

Fig. 13. (a) Nyquist plots of Faradaic impedance at various δ_c (circle: 2×10^{-3} cm; square: 3×10^{-3} cm; triangle: 4×10^{-3} cm) and (b) I–E_c curves at various δ_c (the solid line: 2×10^{-3} cm, the gray line: 3×10^{-3} cm and the dashed line: 4×10^{-3} cm) of the counter electrode. The parameter values excepting δ_c for the calculations are written in Table 2.

3.4. Faradaic Impedance and I–E_c curve of counter electrode

Fig. 12(a) shows Faradaic impedance of the counter electrode ($Z_{F,c}$) calculated with Eqs. (46), (51) and (52). Table 2 shows the simulation parameters for $Z_{F,c}$. The DC potential of the counter electrode is set at E_{eq}-20 mV (represented as $E_{eq\text{-}20}$) in the Faradaic impedance simulation where E_{eq} is the equilibrium potential at I = 0 A in the I–E_c curve. The $Z_{F,c}$ shows the locus of the finite diffusion impedance. The resistances in high and low frequency limits are represented as the symbols $R_{h,c}$ and $R_{l,c}$, respectively, in Fig. 12(a). The $R_{h,c}$ and $R_{diff,c}$ are derived from Eq. (46) as follows.

$$R_{h,c} = \frac{1}{2F(-b_3k_3\bar{c}_{I_3^-,c} + b_{-3}k_{-3}\bar{c}^3_{I^-,c})} \tag{59}$$

$$R_{l,c} = \frac{1+\delta_c((1/D_{I_3^-})k_3 + (9/D_{I^-})k_{-3}\bar{c}^2_{I^-,c})}{2F(-b_3k_3\bar{c}_{I_3^-,c} + b_{-3}k_{-3}\bar{c}^3_{I^-,c})} \tag{60}$$

Table 2
The parameters list to calculate Faradaic impedance and I–E_c curve of the counter electrode in Fig. 12.

Parameter	Value
D_{I^-} [cm^2 s^{-1}]	10^{-5}
$D_{I_3^-}$ [cm^2 s^{-1}]	10^{-5}
$c^*_{I^-,a}$ [mol cm^{-3}]	5×10^{-4}
$c^*_{I_3^-,a}$ [mol cm^{-3}]	5×10^{-5}
δ_c [cm]	0.002
k_3' [cm s^{-1}]	0.01
k_{-3}' [cm^7 mol^{-2} s^{-1}]	0.01
b_3 [V^{-1}]	−40
b_{-3} [V^{-1}]	40
h_3 [cm]	10^{-7}

In addition, the diffusion resistance of the counter electrode $R_{diff,c}$ can be obtained by subtracting $R_{h,c}$ from $R_{l,c}$.

$$R_{diff,c} = \frac{\delta_c((1/D_{I_3^-})k_3 + (9/D_{I^-})k_{-3}\bar{c}^2_{I^-,c})}{2F(-b_3k_3\bar{c}_{I_3^-,c} + b_{-3}k_{-3}\bar{c}^3_{I^-,c})} \tag{61}$$

Fig. 12(b) shows the I–E_c curve calculated with the parameters in Table 2. The absolute value of current increases under charge transfer control at low overvoltage and takes almost constant value under diffusion limiting control at high overvoltage.

Fig. 13 shows the calculated results of $Z_{F,c}$ and I–E_c curves with the variation of δ_c. The $R_{diff,c}$ increases with the increase of δ_c since the fluxes of I^- and I_3^- decrease with the increase of δ_c. This result is in good agreement with Eq. (61). In Fig. 13(b), the diffusion limiting current is observed in the high overvoltage region. The diffusion limiting current decreases with the increase of δ_c since the diffusion-limited current is inversely proportionate to δ_c.

Fig. 14(a) shows the $R_{h,c}$ calculated with Eq. (59) with the variations of $D_{I_3^-}$ and D_{I^-}. Beside, Fig. 14(c) and (d) shows the $\bar{c}_{I_3^-,c}$ and $\bar{c}_{I^-,c}$, respectively, calculated with the variations of $D_{I_3^-}$ and D_{I^-}. The $R_{h,c}$ decreases with the increase of $D_{I_3^-}$ because the $\bar{c}_{I_3^-,c}$ increases with the increase of $D_{I_3^-}$. On the other hand, the $R_{h,c}$ increases with increase of D_{I^-}. Fig. 14(b) shows the $R_{diff,c}$ calculated with Eq. (59) with the variations of $D_{I_3^-}$ and D_{I^-}.The $R_{diff,c}$ decreases with the increase of both $D_{I_3^-}$ and D_{I^-}. This result indicates that both diffusion processes contribute to the reduction on the counter electrode.

3.5. I–V curve of DSC

When the current I flows through the DSC, the absolute value of the anodic current of the photoelectrode is equal to that of the

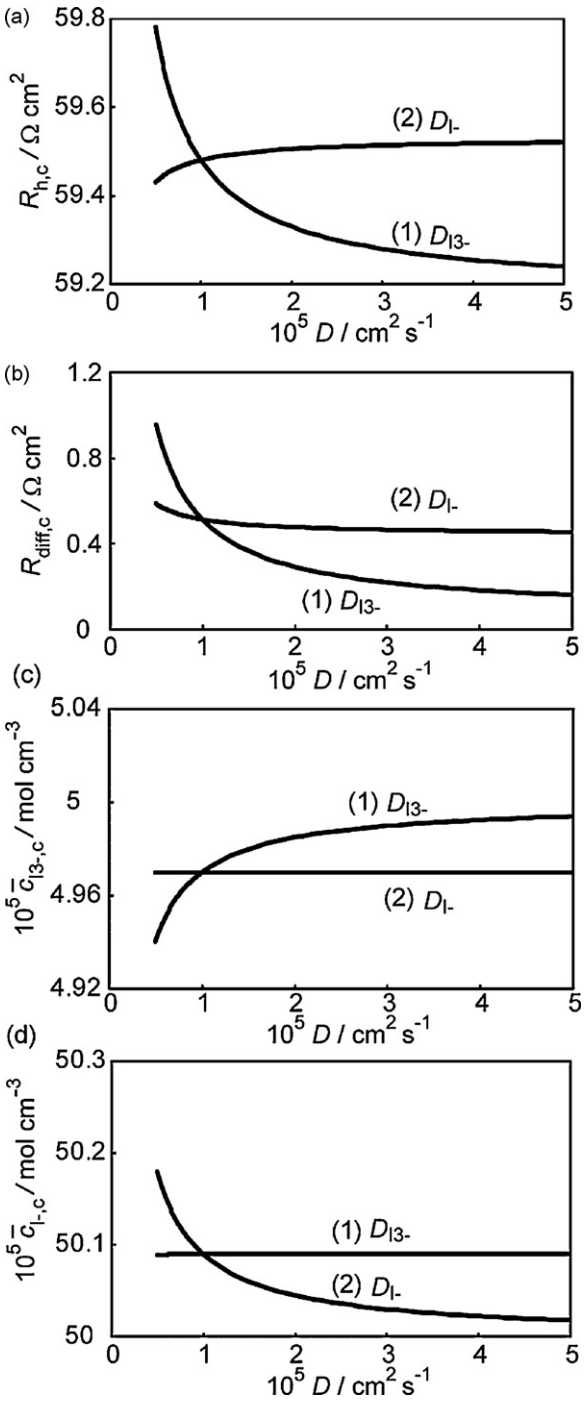

Fig. 14. Influences of diffusion coefficients on (a) $R_{m,c}$, (b) $R_{diff,a}$, (c) $\bar{c}_{I_3^-,c}$ and (d) $\bar{c}_{I^-,c}$. The curves indicated by (1) and (2) are the results with the variations of $D_{I_3^-}$ and D_{I^-}, respectively. The parameter values excepting $D_{I_3^-}$ and D_{I^-} for the calculations are written in Table 2.

cathodic current of the counter electrode. The anodic current of the photoelectrode and the cathodic current of the counter electrode can be calculated by Eqs. (12) and (44), respectively. The overvoltages of the photoelectrode and the counter electrode are represented as $\eta_a(I)$ and $\eta_c(I)$, respectively. In the present paper, η_a can be regarded as the potential of the photoelectrode (E_a). The η_c is calculated by the following equation:

$$\eta_c = E_c - E_{eq}, \tag{62}$$

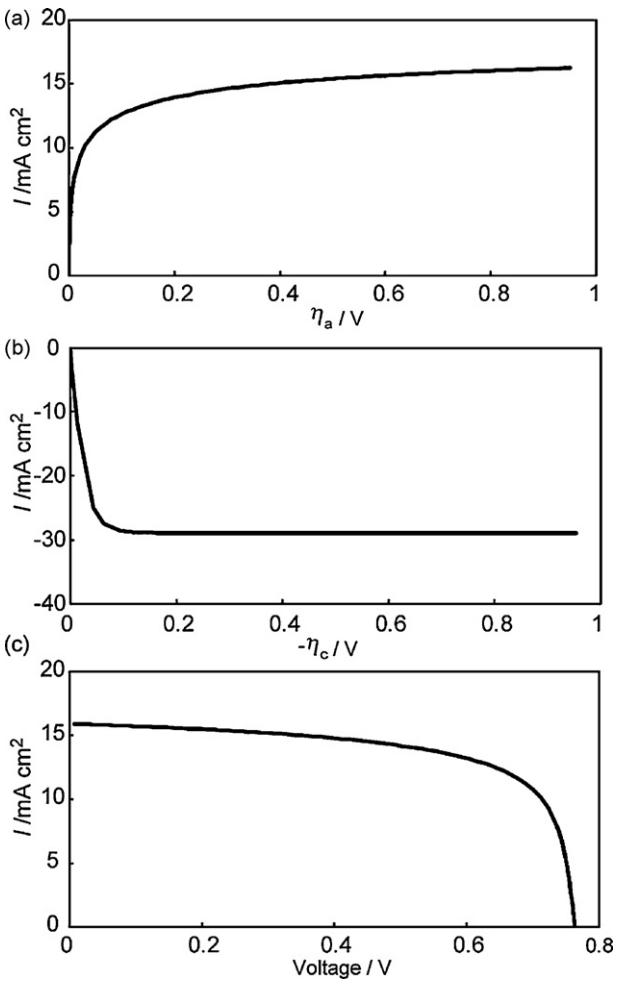

Fig. 15. (a) I–η_a curve of photoelectrode, (b) I–η_c curve of counter electrode and (c) I–V curve of DSC calculated with the parameters in Table 3.

where E_{eq} is the equilibrium potential of the counter electrode at $I = 0$ A in I–E_c curve.The voltage of the DSC is symbolized as $V(I)$. The $V(I)$ is calculated by following equation:

$$V(I) = V_{oc} - (\eta_a(I) - \eta_c(-I) - R_s I), \tag{63}$$

where R_s is the total resistance of the substrate and solution. In addition, the open circuit voltage V_{oc} must be determined in order to simulate the I–V curves. The theoretical equation of V_{oc} was reported by Koelsh et al. [116] as below:

$$V_{oc} = \frac{RT}{F} \ln \left\{ \frac{(1-\bar{\theta})G_0}{k_2 \bar{c}_{I_3^-} N_0} \right\}, \tag{64}$$

where N_0 is the electron density in the TiO_2 film surface when $V_{oc} = 0$, T is the absolute temperature and R is the gas constant. In addition, the I–V curves are calculated under following assumptions in this section.

(A) $\delta_a = \delta_c$
(B) The thickness of the cell = $\delta_a + \delta_c$
(C) $D_{I^-} = D_{I_3^-}$
(D) $c^*_{I^-,a} = c^*_{I^-,c}$ and $c^*_{I_3^-,a} = c^*_{I_3^-,c}$

Fig. 15 shows the I–η_a curve of the photoelectrode, I–η_c curve of the counter electrode and I–V curve of the DSC. The parameter values for the calculation in Fig. 15 are shown in Table 3. In the I–η_a curve shown in Fig. 15(a), the anodic current increases

Table 3
The parameters list to calculate impedance, I–η_a, I–η_c and I–V curves in Figs. 15, 17 and 21.

Parameter	Value	Ref.
κ_s [F cm^{-1}]	4.43×10^{-12}	
D_{I^-} [cm^2 s^{-1}]	10^{-5}	[25]
$D_{I_3^-}$ [cm^2 s^{-1}]	10^{-5}	[25]
T [K]	300	
$c^*_{I^-,a}$ [mol cm^{-3}]	3×10^{-4}	
$c^*_{I_3^-,a}$ [mol cm^{-3}]	3×10^{-5}	
G_0 [mol cm^{-2} s^{-1}]	2×10^{-7}	
D_e [cm^2 s^{-1}]	5×10^{-5}	[105]
k_1 [cm^7 mol^{-2} s^{-1}]	10^9	
k_2 [cm^4 mol^{-1} s^{-1}]	10^5	
N_D [cm^{-3}]	10^{16}	
δ_a [cm]	0.002	
n_0 [mol cm^{-2}]	10^{-8}	
h_1,h_2 [cm]	10^{-7}	
$c^*_{I^-,c}$ [mol cm^{-3}]	3×10^{-4}	
$c^*_{I_3^-,c}$ [mol cm^{-3}]	3×10^{-5}	
δ_c [cm]	0.002	
k_3' [cm s^{-1}]	10	
k_{-3}' [cm^7 mol^{-2} s^{-1}]	10	
b_3 [V^{-1}]	−40	
b_{-3} [V^{-1}]	40	
h_3 [cm]	10^{-7}	
R_s [Ω cm^2]	1	
N_0 [mol cm^{-3}]	10^{-20}	
$C_{dl,a}$ [F cm^{-2}]	5×10^{-3}	
$C_{dl,c}$ [F cm^{-2}]	10^{-4}	

in the low overpotential region and takes nearly constant value (about 15 mA cm^{-2}) in the high overpotential region. Fig. 15(b) shows the I–η_c curve calculated with Eq. (44) while substituting $\bar{c}_{I^-,c}$ in Eq. (40) and $\bar{c}_{I_3^-,c}$ in Eq. (41) into $c_{I^-,c}$ and $c_{I_3^-,c}$, respectively, in Eq. (44). In I–η_c curve, the cathodic current sharply increases in the low overpotential region and takes constant value (about 28 mA cm^{-2}) in the high overpotential region. The sufficiently large value of k_3 is selected to simulate the electrochemical nature of the counter electrode with high catalytic performance in Fig. 15(b). Fig. 15(c) shows the I–V curve of the DSC calculated with Eq. (63) from the results in Fig. 15(a) and (b). The general shape of I–V curve for DSC could be simulated in Fig. 15(c). In addition, it is found that I–V curve has left–right symmetry against the I-η_a curve and that the shape of I–V curve is governed by the performance of photoelectrode.

The electrical energy conversion efficiency and fill factor can be calculated from the I–V curve. In order to calculate the electrical energy conversion efficiency, the relation between G_0 and light intensity must be estimated. The light intensity at a single wavelength λ of the photon ($I_0(\lambda)$) is represented as follows:

$$I_0(\lambda) = \left(\frac{E_s(\lambda)}{E_\lambda N_A}\right), \tag{65}$$

$$E_\lambda = h\frac{c_0}{\lambda}, \tag{66}$$

where h is the Planck constant, c_0 is the light speed, N_A is Avogadro's number, $E_s(\lambda)$ is the light intensity at λ under the reference solar spectral irradiance and E_λ is the energy per one photon at λ. The G_0 can be calculated by the integration of Eq. (65) with following equation:

$$G_0 = h_2\phi\int_{\lambda_1}^{\lambda_2}\alpha_{abs}(\lambda)I_0(\lambda)d\lambda, \tag{67}$$

where ϕ is the effective permeability of light of the photoelectrode and $\alpha_{abs}(\lambda)$ is the absorption coefficient of the dye at λ. The total light intensity is assumed as 100 mW cm^{-2}. For example, when the DSC generates the electricity by the light irradiation from

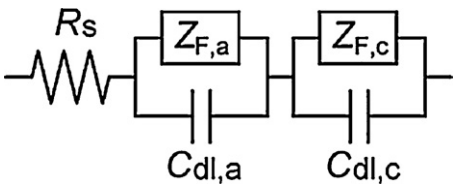

Fig. 16. The equivalent circuit of DSC with Faradaic impedance. R_s is total resistance of the substrate and solution. $Z_{F,a}$ and $Z_{F,c}$ are the Faradaic impedance of the photoelectrode and the counter electrode, respectively. $C_{dl,a}$ and $C_{dl,c}$ are the electric double layer capacitance of the photoelectrode and the counter electrode, respectively.

350 to 900 nm, G_0 is calculated as 2.7×10^{-7} mol cm^{-2} s^{-1} assuming that $\alpha_{abs}(\lambda) = 10^3$ cm^{-1}, $\phi = 1$ and $h_2 = 10^{-7}$ cm. The G_0 is set to 2.0×10^{-7} mol cm^{-2} s^{-1} for the light intensity of 100 mW cm^{-2} for the calculations in Fig. 15, and the energy conversion efficiency can be estimated as 8.0% for the I–V curve in Fig. 15(c). In addition, the

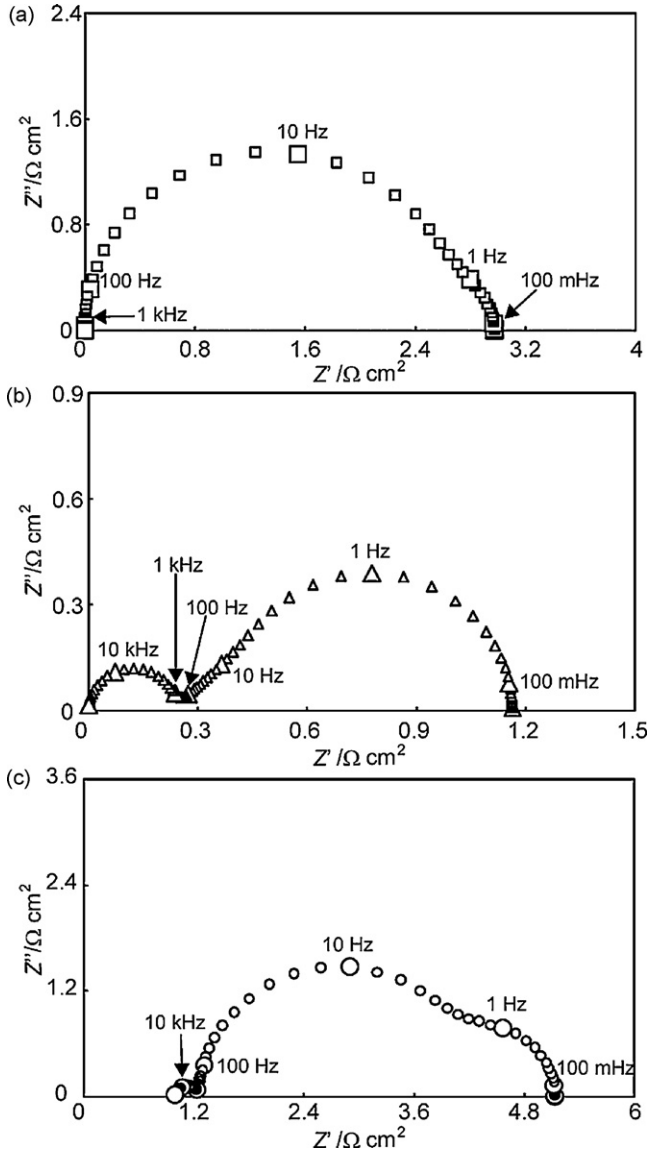

Fig. 17. Impedance spectra of (a) photoelectrode, (b) counter electrode and (c) DSC calculated with the parameters in Table 3. R_s is 1 Ω. Procedure to decide the overvoltages of photoelectrode and counter electrode are as follows: (1) a current of I–V curve in Fig. 15(c) was decided at $V = V_{oc} - 0.02$ V, (2) the $\eta_a(I)$ of photoelectrode was decided by I–η_a in Fig. 15(a) at I by (1), and (3) the $\eta_c(I)$ of counter electrode was decided by I–η_a in Fig. 15(b) at the absolute value of I by (1).

fill factor estimated by the geometry of *I–V* curve in Fig. 15(c) is 0.66.

3.6. Cell impedance obtained from Faradaic impedance

Fig. 16 shows the equivalent circuit of the cell impedance Z_{DSC} proposed in the present The equivalent circuit in Fig. 16 is composed of the five parameters as follows: total resistance of the substrate and solution (R_s), the Faradaic impedance of the photoelectrode ($Z_{F,a}$) and the counter electrode ($Z_{F,c}$), the electric double layer capacitance of the photoelectrode ($C_{dl,a}$) and the counter electrode ($C_{dl,c}$).

The following equations allow the impedance of the photoelectrode Z_a and the counter electrode Z_c.

$$Z_a = \frac{Z_{F,a}}{j\omega Z_{F,a} C_{dl,a} + 1} \tag{68}$$

$$Z_c = \frac{Z_{F,c}}{j\omega Z_{F,c} C_{dl,c} + 1} \tag{69}$$

The cell impedance Z_{DSC} can be calculated according to the equivalent circuit in Fig. 16 as below.

$$Z_{DSC} = Z_a + Z_c + R_s \tag{70}$$

If AC voltage is imposed to the DSC at V_{oc}, the cell voltage exceeds the V_{oc} alternately, resulting in the reverse current through the cell. In the practical experiment, the smaller DC voltage than V_{oc} should be used to measure the impedance of DSC to avoid the alternate reverse current. Thus the DC voltage is set to V_{oc}-20 mV (represented as $V_{oc\text{-}20}$) for the simulations in Figs. 17 and 20.

Fig. 17 shows the Nyquist plots of the Z_a, Z_c and Z_{DSC} at $V_{oc\text{-}20}$ calculated by using the parameters shown in Table 3. The impedance Z is represented by real part Z' and imaginary part Z'' with the relation of $Z = Z' - jZ''$. In Fig. 17(a), Z_a describes locus of semicircle in the high frequency range and locus of a portion of finite diffusion impedance in the low frequency range. In Fig. 17(b), the Z_c describes locus of semicircle in the high range and locus of the finite diffusion impedance in the low frequency range. In Fig. 17(c), Z_{DSC} describes three semicircles on the Nyquist plane. The impedance spectrum of Z_{DSC} is in good agreement with that of the typical experimental results reported previously [9,18].

Fig. 18 shows the schematic illustrations of the relations of equivalent circuits and impedance spectra. The shapes of the impedance spectra shown in Fig. 17 are discussed by relating to the schematic illustrations shown in Fig. 18. Concerning the impedance of photoelectrode, almost all the current passes through only $C_{dl,a}$ above 10 kHz since the capacitive reactance ($1/\omega C_{dl,a}$) due to $C_{dl,a}$ is quite small in comparison with $Z_{F,a}$ in the high frequency range. Therefore, the Z_a converges at origin of Nyquist plane above 1 kHz. The Z_a describes semicircle and finite diffusion impedance, however the boundary between two loci is not clear. The time constant of the semicircle $\tau_{semi,a}$ in Fig. 18 is calculated as follows.

$$\tau_{semi,a} = R_{m,a} C_{dl,a} \tag{72}$$

The semicircle of Z_a is different from the portion of semicircle of $Z_{F,a}$. The portion of $Z_{F,a}$ is hided by the semicircle of Z_a because the $\tau_{h,a}$ in Eq. (55) is much smaller than $\tau_{semi,a}$. On the other hand, the time constant of the finite diffusion impedance $\tau_{l,a}$ in Fig. 18 is represented by Eq. (58). In Fig. 17(a), $\tau_{semi,a}$ and $\tau_{l,a}$ are calculated as 0.013 s and 0.4 s, respectively. Since the difference between $\tau_{semi,a}$ and $\tau_{l,a}$ is small, the loci of the semicircle and the diffusion impedance of Z_a are not separated clearly. The diameter of semicircle of Z_a is $R_{m,a}$, and $R_{m,a}$ can be interpreted by the charge transfer resistance of the photoelectrode.

The semicircle of Z_c in Fig. 17(b) is related to $R_{h,c}$ and $C_{dl,c}$. The time constant of the semicircle $\tau_{semi,c}$ is represented as below.

$$\tau_{semi,c} = R_{h,c} C_{dl,c} \tag{73}$$

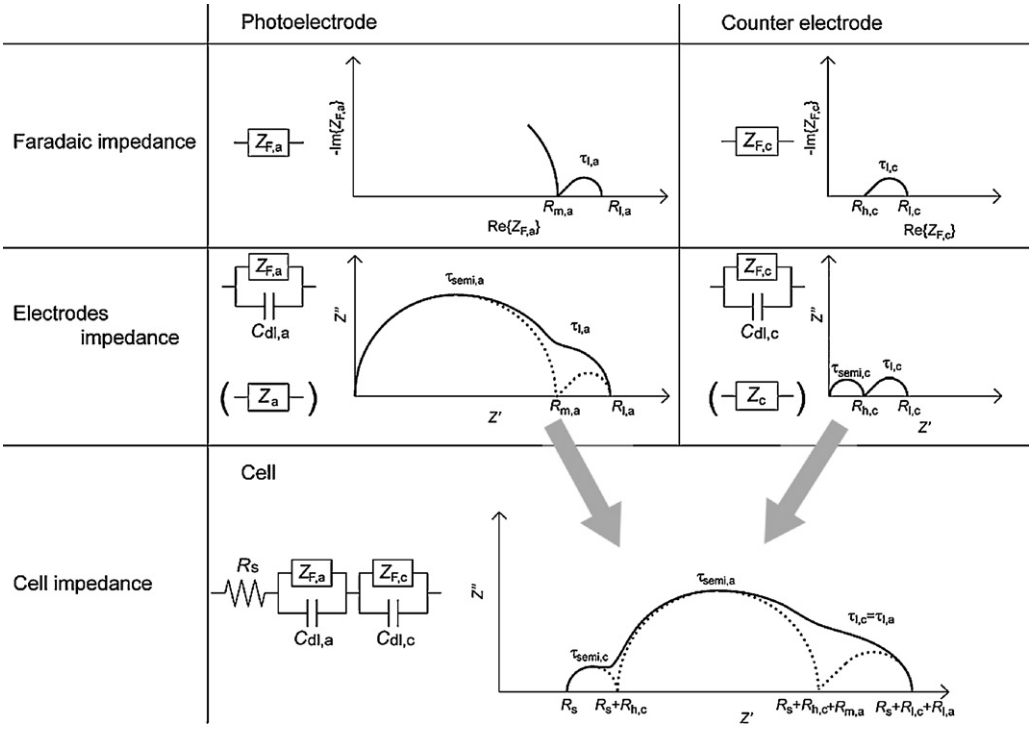

Fig. 18. The schematic illustrations to present the relations between the equivalent circuits and impedance spectra.

The time constant of the finite diffusion impedance ($\tau_{l,c}$) is described by following equation.

$$\tau_{l,c} = \frac{(\delta_c)^2}{D_{I_3^-}} \tag{74}$$

The $\tau_{semi,c}$ and $\tau_{l,c}$ are calculated as 2.2×10^{-5} and 0.4 s, respectively, in Fig. 17(b). Since the $\tau_{semi,c}$ is sufficiently different from that of $\tau_{l,c}$, the loci of the semicircle and that of the finite diffusion impedance are separated clearly.

The spectrum of Z_{DSC} is sum of those of Z_a, Z_c and R_s. The order of time constant is $\tau_{l,a} = \tau_{l,c} > \tau_{semi,a} > \tau_{semi,c}$ in Fig. 17. Thus, the semicircles in the high frequency range are attributed to $R_{h,c}$ and $C_{dl,c}$. The semicircle in the middle frequency range is attributed to $R_{m,a}$ and $C_{dl,a}$. From these results, the following relations are obtained by comparing the equivalent circuit in Fig. 16 with that in Fig. 1(a).

$$R_{ct,1} = R_{h,c} = \frac{1}{2F(-b_3 k_3 \bar{c}_{I_3^-,c} + b_{-3} k_{-3} \bar{c}^3_{I^-,c})} \tag{75}$$

$$R_{ct,2} = R_{m,a} = \frac{2}{F\mu\bar{n}_s}\sqrt{\frac{\kappa_s(E_a - E_{fb})}{2qN_D}} + \frac{E_a - E_{fb}}{Fk_2\bar{c}_{I_3^-,a}\bar{n}_s} \tag{76}$$

In the present study, the physical meanings of $R_{ct,1}$ and $R_{ct,2}$ can be discussed by the interpretations of Faradaic impedance. The $R_{ct,1}$ is represented as the function of the potential-dependent rate constants of I_3^- reduction and I^- oxidation. On the other hand, the $R_{ct,2}$ is the function of the photoelectrode potential, the surface concentration of I_3^- and the potential-independent rate constant of the back electron transfer reaction.

The impedance in the low frequency range is due to the sum of the finite diffusion impedance of the photoelectrode and the counter electrode since $\tau_{l,a} = \tau_{l,c}$. In the case of the typical equivalent circuit shown in Fig. 1(a), it has been considered that the finite diffusion impedance Z_w is due to the diffusion of I_3^- on the counter electrode [34,35]. However, it can be proved that the semicircle of Z_{DSC} in the low frequency range is attributed to the diffusion of I_3^- on the both photoelectrode and counter electrode. The following relation regarding the diffusion resistance of Z_{DSC} (Z_w ($\omega \to 0$ s^{-1})) is derived by comparing the equivalent circuits shown in Fig. 1(a) and Fig. 16.

$$Z_w(\omega \to 0\,s^{-1}) = R_{diff,a} + R_{diff,c} \tag{77}$$

The $R_{diff,a}$ is estimated about 0.3 Ω in Fig. 17(a). Meanwhile, the $R_{diff,c}$ is about 0.9 Ω in Fig. 17(b). Therefore, the contribution ratio of the photoelectrode and counter electrode to Z_w ($\omega \to 0$ s^{-1}) is estimated as 1:3, respectively, in Fig. 17(c).

3.7. Relation between impedance and I–V curve

The relations between the *I–V* curve in Fig. 15(c) and the impedance spectrum in Fig. 16(c) is discussed firstly in this section. The polarization resistance R_p is defined by the low frequency limit of Z_{DSC}, and R_p is represented as below.

$$R_p = R_s + R_{l,c} + R_{l,a} \tag{78}$$

Beside, the R_p is equal to the reciprocal of the *I–V* curve gradient. The performance of the DSC is improved by increasing the fill factor. It is generally considered that the fill factor increases with the increase of the *I–V* curve gradient at nearly V_{oc}. Thus, it is important for the improvement of the performance of the DSC to decrease the R_p. In Fig. 17(c), the value of R_p depends on $R_{m,a}$ significantly because the parameters are selected to simulate high perfprmance counter electrode. The $R_{m,a}$ is the function of the photoelectrode potential E_a, the surface concentration of I_3^- $c_{I_3^-}$ and the potential-independent rate constant of the back electron transfer reaction k_2. For example in Fig. 8, the $R_{m,a}$ increases with the increase of k_2 above 10^5 cm^4 mol^{-1} s^{-1}.

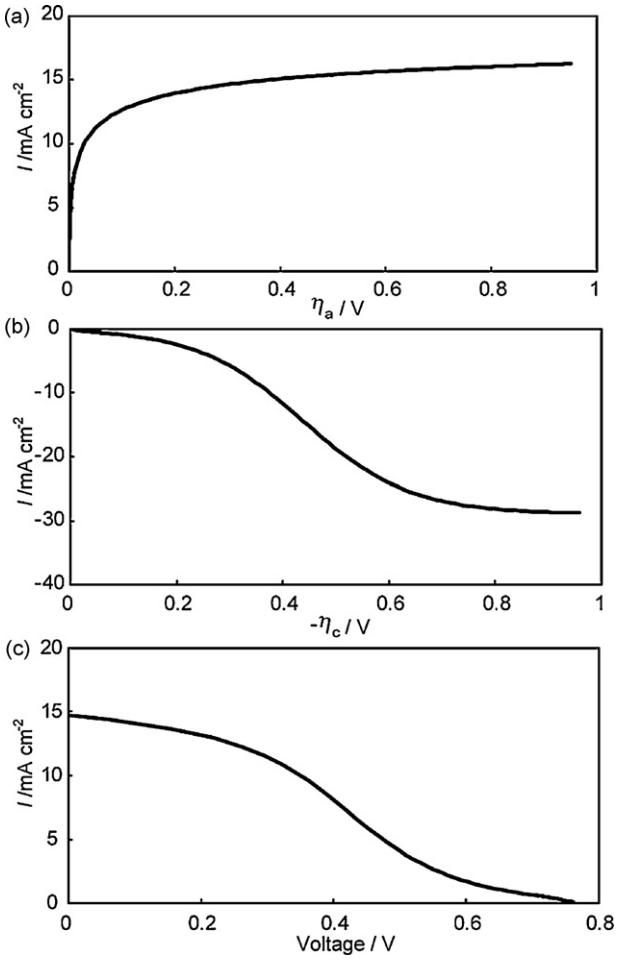

Fig. 19. (a) I–η_a curve of photoelectrode, (b) I–η_c curve of counter electrode and (c) *I–V* curve of DSC calculated with the parameters in Table 3 excepting k_3' and b_3. The k_3' and b_3 are 10^{-4} cm s^{-1} and -10 V^{-1}, respectively.

The relation between *I–V* curve and impedance spectra of the DSC is discussed in the case that the performance of the counter electrode are lower than that in Figs. 15 and 17. For example, a carbon electrode has less catalytic ability than a platinum electrode generally. Fig. 19 shows the I–η_a curve, I–η_c curve and *I–V* curve in this case. The I–η_a curve in Fig. 19(a) is same as that in Fig. 15(a) since it is calculated by using the same parameters for photoelectrode in Table 3. The gradient of the I–η_c curve in Fig. 19(b) is small in the low overvoltage region comparing with that in Fig. 15(b), since the cathodic current in the low overvoltage region is related to k_3 that is the potential-dependent parameter. Therefore, it is considered that the shape of the *I–V* curves is governed by the performance of the counter electrode in the low overvoltage region. Meanwhile, the absolute value of current of the counter electrode in Fig. 19(b) is larger than that of the photoelectrode in Fig. 19(a) in the high overvoltage. Fig. 19(c) shows the *I–V* curve calculated with Eq. (63) from the results in Fig. 19(a) and (b). The shape of the *I–V* curves is governed by the shape of the counter electrode in this case. The shape of the *I–V* curve in Fig. 19(c) have been observed at the DSC in which alternative counter electrodes was used instead of Pt [117]. The energy conversion efficiency and fill factor of the DSC in Fig. 19(c) are estimated as 0.32 and 3.5%, respectively. The Nyquist plots of the Z_a and Z_c are shown in Fig. 20(a) and (b). Fig. 20(c) shows the Nyquist plot of

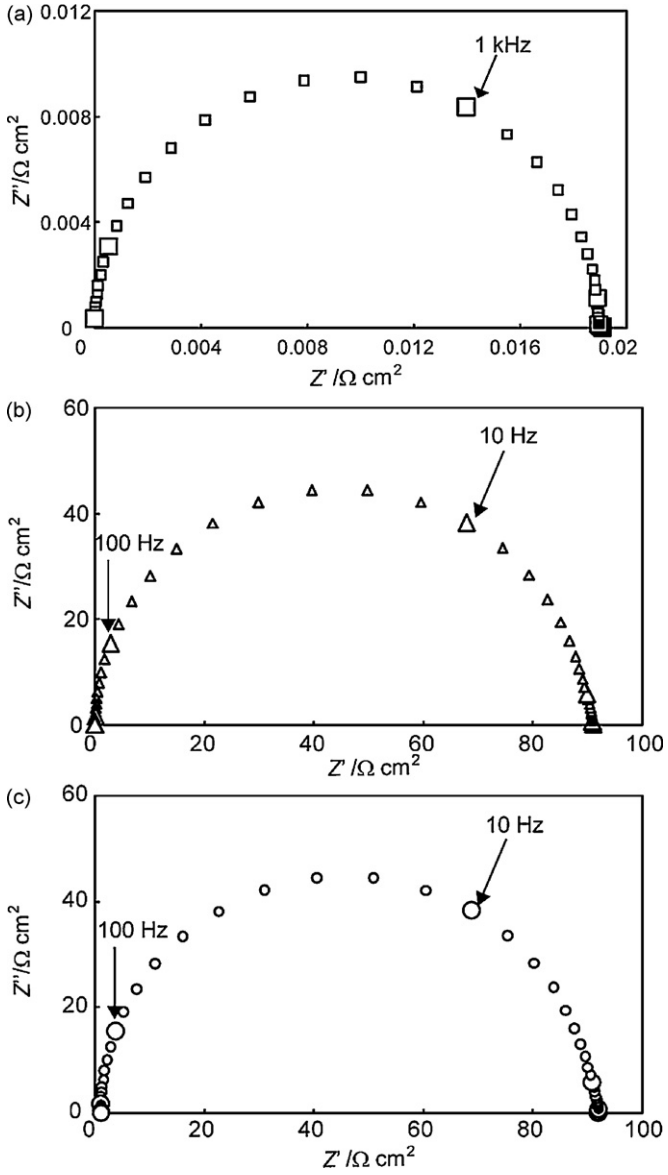

Fig. 20. Impedance spectra of (a) photoelectrode, (b) counter electrode and (c) DSC calculated with the parameters in Table 3 excepting k_3' and b_3. The k_3' and b_3 are 10^{-4} cm s^{-1} and -10 V^{-1}, respectively. R_s is 1 Ω. Procedure to decide the overvoltages of photoelectrode and counter electrode are as follows: (1) a current of I–V curve in Fig. 19(c) was decided at $V = V_{oc} - 0.02$ V, (2) the $\eta_a(I)$ of photoelectrode was decided by I–η_a in Fig. 19(a) at I by (1), and (3) the $\eta_c(I)$ of counter electrode was decided by I–η_a in Fig. 19(b) at the absolute value of I by (1).

the Z_{DSC} at $V_{oc\text{-}20}$. The Z_a is much smaller than Z_c in all frequency range. Therefore, the Z_{DSC} is nearly identical to that of Z_c. R_p is almost equal to $R_{l,c}$ of the counter electrode. In this case, the performance of the DSC cell is governed by the performance of the counter electrode.

Fig. 21 shows the I–V curves with the variation of R_s. The gradient of I–V curve increases with the increase of R_s in the low overvoltage region. The fill factors are estimated as 0.68 at 0 Ω, 0.62 at 5 Ω, 0.56 at 10 Ω and 0.29 at 50 Ω. As above-mentioned, the reciprocal of the I–V curve gradient at V_{oc} is equal to R_p. The R_p depends on R_s significantly when R_s is much larger than $R_{l,c}$ and $R_{l,a}$. In the case that $R_s = 50$ Ω, the shape of I–V curve is close to the linear since the I–V curves is governed by Ohm's law. From these results, it can be concluded that decrease of R_s is very important factor for the improvement of the DSC performance.

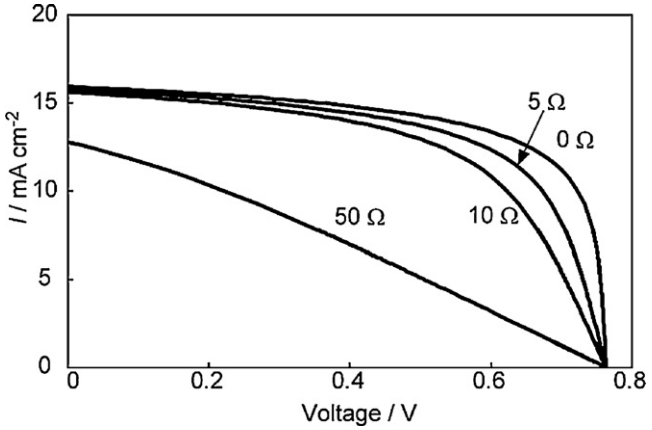

Fig. 21. The influence of the R_s on I–V curves of DSC calculated with the parameters in Table 3.

4. Conclusions

The theoretical equations of the Faradaic impedance of the photoelectrode and the counter electrode of dye-sensitized solar cell (DSC) were derived. The relation of the cell impedance and the current–voltage (I–V) curve was discussed. The typical cell impedance spectrum describes three semicircles which is generally analyzed by using the equivalent circuit composed of charge transfer resistance ($R_{ct,1}$) and capacitance ($C_{dl,1}$) of counter electrode, charge transfer resistance ($R_{ct,2}$) and capacitance ($C_{dl,2}$) of photoelectrode, the finite diffusion impedance due to the diffusion of I_3^- on the counter electrode (Z_w), and total resistance of the substrate and solution (R_s). In the present study, the physical meanings of $R_{ct,1}$ and $R_{ct,2}$ can be elucidated by the interpretations of Faradaic impedance as follows.

$$R_{ct,1} = \frac{1}{2F(-b_3 k_3 \bar{c}_{I_3^-,c} + b_{-3} k_{-3} \bar{c}^3_{I^-,c})}$$

$$R_{ct,2} = \frac{2}{F\mu\bar{n}_s}\sqrt{\frac{\kappa_s(E_a - E_{fb})}{2qN_D}} + \frac{E_a - E_{fb}}{Fk_2\bar{c}_{I_3^-,a}\bar{n}_s}$$

In addition, it is proved that the finite diffusion impedance Z_w in the low frequency range is attributed to the diffusion of I_3^- on the both photoelectrode and counter electrode.

Appendix A.

Poisson's equation is written as below, considering that the charge of qN_DW exists in the space charge layer ($0 < x < W$).

$$\frac{\partial^2\phi}{\partial x^2} = -\frac{qN_D}{\kappa_s} \quad \text{(A-1)}$$

In Eq. (A-1), ϕ is the potential at the position x. Three boundary conditions are as follows.

$$\left.\frac{\partial\phi}{\partial x}\right|_{x=W} = 0 \quad \text{(A-2)}$$

$$\phi(0) = E_{fb} \quad \text{(A-3)}$$

$$\phi(W) = E_a \quad \text{(A-4)}$$

Integration of Eq. (A-1) and the boundary condition (A-2) give the following equation.

$$\left.\frac{\partial\phi}{\partial x}\right|_{x=W} = -\frac{qN_D}{\kappa_s}x + \frac{qN_D}{\kappa_s}W = 0 \quad \text{(A-5)}$$

Furthermore, integration of Eq. (A-5) and the boundary condition (A-3) give the following equation.

$$\phi = -\frac{qN_D}{2\kappa_s}x^2 + \frac{qN_D}{\kappa_s}Wx + E_{fb} \tag{A-6}$$

From the boundary condition (A-4):

$$\phi(W) = \frac{qN_D}{2\kappa_s}W^2 + E_{fb} = E_a. \tag{A-7}$$

Transformation of Eq. (A-7) allows the expression of W as below.

$$W = \sqrt{\frac{2\kappa_s(E_a - E_{fb})}{qN_D}} \tag{A-8}$$

The electric field $\vec{E}$ at $x = 0$ is represented as below.

$$\vec{E} = \left.\frac{\partial\phi}{\partial x}\right|_{x=0} = \frac{qN_D}{\kappa_s}W \tag{A-9}$$

Thus Eq. (7) can be obtained by substituting Eq. (A-8) into Eq. (A-9).

$$\vec{E} = \sqrt{\frac{2qN_D(E_a - E_{fb})}{\kappa_s}} \tag{7}$$

Appendix B.

Newton–Raphson method is used to analyze nonlinear partial differential equations. This method assumes the function $f(x)$ to have a continuous first derivative near $x = x_n$ .With x_0 as the initial guess, x_1 is calculated from Eq. (B-1).

$$x_1 = x_0 - \frac{f(x_0)}{f'(x_0)} \tag{B-1}$$

The process is repeated until a sufficiently accurate value is reached.

$$x_{k+1} = x_k - \frac{f(x_k)}{f'(x_k)} \tag{B-2}$$

The relation among the parameters in Eq. (2) is described in Fig. A1. When the calculation is repeated n times, the approximate solution (x_n) can be calculated.

In the present paper, the approximate values of the $\bar{c}_{I_3^-,a}$ $\bar{c}_{I^-,a}$, $\bar{\theta}$ and $\bar{n}_s$ are estimated from the following four equations by using the Newton–Raphson method.

$$f_1(\bar{c}_{I^-,a}, \bar{c}_{I_3^-,a}\bar{\theta}, \bar{n}_s) = -3k_1\bar{c}_{I^-,a}^3\bar{\theta}^2 + 3k_2\bar{n}_s\bar{c}_{I_3^-,a} + \frac{D_{I^-}(c^*_{I^-,a} - \bar{c}_{I^-,a})}{\delta_a} \tag{8'}$$

$$f_2(\bar{c}_{I^-,a}, \bar{c}_{I_3^-,a}\bar{\theta}, \bar{n}_s) = k_1\bar{c}_{I^-,a}^3\bar{\theta}^2 - k_2\bar{n}_s\bar{c}_{I_3^-,a} + \frac{D_{I_3^-}(c^*_{I_3^-,a} - \bar{c}_{I_3^-,a})}{\delta_a} \tag{9'}$$

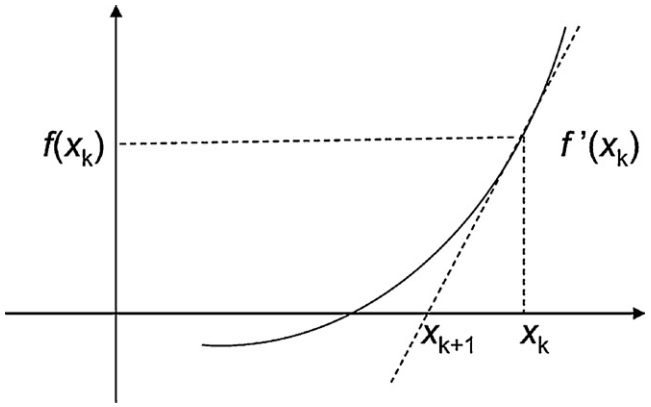

Fig. A1. The model of Newton's method.

$$f_3(\bar{c}_{I^-,a}, \bar{c}_{I_3^-,a}\bar{\theta}, \bar{n}_s) = (1-\bar{\theta})G_0 - 2k_1\bar{c}_{I^-,a}^3\bar{\theta}^2 \tag{10'}$$

$$f_4(\bar{c}_{I^-,a}, \bar{c}_{I_3^-,a}\bar{\theta}, \bar{n}_s) = (1-\bar{\theta})G_0 - 2k_2\bar{n}_s\bar{c}_{I_3^-,a} - \bar{n}_s\mu\sqrt{\frac{2qN_D(E_a - E_{fb})}{\kappa_s}} \tag{11'}$$

Jacobian determinant which is derived from four equations is shown as follows:

$$J = \begin{bmatrix} \frac{\partial f_1}{\partial \bar{c}_{I^-,a}} & \frac{\partial f_1}{\partial \bar{c}_{I_3^-,a}} & \frac{\partial f_1}{\partial \bar{\theta}} & \frac{\partial f_1}{\partial n_s} \\ \frac{\partial f_2}{\partial \bar{c}_{I^-,a}} & \frac{\partial f_2}{\partial \bar{c}_{I_3^-,a}} & \frac{\partial f_2}{\partial \bar{\theta}} & \frac{\partial f_2}{\partial n_s} \\ \frac{\partial f_3}{\partial \bar{c}_{I^-,a}} & \frac{\partial f_3}{\partial \bar{c}_{I_3^-,a}} & \frac{\partial f_3}{\partial \bar{\theta}} & \frac{\partial f_3}{\partial n_s} \\ \frac{\partial f_4}{\partial \bar{c}_{I^-,a}} & \frac{\partial f_4}{\partial \bar{c}_{I_3^-,a}} & \frac{\partial f_4}{\partial \bar{\theta}} & \frac{\partial f_4}{\partial n_s} \end{bmatrix} = \begin{bmatrix} -9k_1\bar{c}_{I^-,a}^2\bar{\theta}^2 - \frac{D_{I^-}}{\delta_a} & 3k_2\bar{n}_s & -6k_1\bar{c}_{I^-,a}^3\bar{\theta} & 3k_2\bar{c}_{I_3^-,a} \\ 3k_1\bar{c}_{I^-,a}^2\bar{\theta}^2 & -k_2\bar{n}_s - \frac{D_{I_3^-}}{\delta_a} & 2k_1\bar{c}_{I^-,a}^3\bar{\theta} & -k_2\bar{c}_{I_3^-,a} \\ -6k_1\bar{c}_{I^-,a}^2\bar{\theta}^2 & 0 & -4k_1\bar{c}_{I^-,a}^3\bar{\theta} - G_0 & 0 \\ 0 & -2k_2\bar{n}_s & -G_0 & -2k_2\bar{c}_{I_3^-,a} - \mu\sqrt{\frac{2qN_D(E_a - E_{fb})}{\kappa_s}} \end{bmatrix} \tag{B-3}$$

The approximate values of the $\bar{c}_{I_3^-,a}$, $\bar{c}_{I^-,a}$, $\bar{\theta}$ and $\bar{n}_s$ can be calculated by Eq. (B-4).

$$\begin{bmatrix} \bar{c}_{I^-,a} \\ \bar{c}_{I_3^-,a} \\ \bar{\theta} \\ \bar{n}_s \end{bmatrix}_{k+1} = \begin{bmatrix} \bar{c}_{I^-,a} \\ \bar{c}_{I_3^-,a} \\ \bar{\theta} \\ \bar{n}_s \end{bmatrix}_{k} - J^{-1}\begin{bmatrix} f_1(\bar{c}_{I^-,a}, \bar{c}_{I_3^-,a}\bar{\theta}, \bar{n}_s) \\ f_2(\bar{c}_{I^-,a}, \bar{c}_{I_3^-,a}\bar{\theta}, \bar{n}_s) \\ f_3(\bar{c}_{I^-,a}, \bar{c}_{I_3^-,a}\bar{\theta}, \bar{n}_s) \\ f_4(\bar{c}_{I^-,a}, \bar{c}_{I_3^-,a}\bar{\theta}, \bar{n}_s) \end{bmatrix} \tag{B-4}$$

This trial was repeated twenty times by using the Microsoft Excel. When the calculated values of $\bar{c}_{I_3^-,a}$, $\bar{c}_{I^-,a}$, $\bar{\theta}$ and $\bar{n}_s$ are substituted in the four equations, the value of every right-hand side of Eqs. (8)′–(11)′ takes under 10^{-22} (= approximately 0). As the result, approximate values of the $\bar{c}_{I_3^-,a}$, $\bar{c}_{I^-,a}$, $\bar{\theta}$ and $\bar{n}_s$ can be obtained.

Appendix C.

Eqs. (26) and (27) can be presented by Eqs. (C-1) and (C-2) assuming that $\omega \to \infty\,s^{-1}$ in the high frequency region.

$$\frac{\Delta c_{I^-,a}}{\Delta J_{I^-,a}} \to 0\,s\,cm^{-1} \text{ at } \omega \to \infty\,s^{-1} \tag{C-1}$$

$$\frac{\Delta c_{I_3^-,a}}{\Delta J_{I_3^-,a}} \to 0\,s\,cm^{-1} \text{ at } \omega \to \infty\,s^{-1} \tag{C-2}$$

Eqs. (C-1) and (C-2) mean that the concentrations of I^- and I_3^- on the photoelectrode don't modulate by the influence of the imposed

AC signal in the high frequency range. Eq. (28) can be written by the simple form as below by substituting Eqs. (C-1) and (C-2).

$$\frac{\Delta n_s}{\Delta E_a} = -\frac{\mu \bar{n}_s \sqrt{2qN_D/\kappa_s(E_a - E_{fb})}}{2(2k_2\bar{c}_{I_3^-,a} + j\omega h_2 + \mu\sqrt{2qN_D(E_a - E_{fb})/\kappa_s})} \quad \text{(C-3)}$$

Furthermore, the semicircle of $Z_{F,a}$ in the high frequency range ($Z_{F,a,h}$) can be obtained by substituting Eq. (C-3) into Eq. (14) as below.

$$Z_{F,a,h} = \frac{2}{F\mu\bar{n}_s}\sqrt{\frac{\kappa_s(E_a - E_{fb})}{2qN_D}} + \frac{(E_a - E_{fb})/Fk_2\bar{c}_{I_3^-,a}\bar{n}_s}{j\omega(h_2/2k_2\bar{c}_{I_3^-,a}) + 1} \quad \text{(C-4)}$$

The time constant of the semicircle presented by Eq. (C-4) is:

$$\tau_{h,a} = \frac{h_2}{2k_2\bar{c}_{I_3^-,a}}. \quad (55)$$

Moreover, the high and low frequency limits of $Z_{F,a,h}$ are written as follows.

$$R_{h,a} = \frac{2}{F\mu\bar{n}_s}\sqrt{\frac{\kappa_s(E_a - E_{fb})}{2qN_D}} \quad (53)$$

$$R_{m,a} = \frac{2}{F\mu\bar{n}_s}\sqrt{\frac{\kappa_s(E_a - E_{fb})}{2qN_D}} + \frac{E_a - E_{fb}}{Fk_2\bar{c}_{I_3^-,a}\bar{n}_s} \quad (54)$$

References

[1] B. O'Regan, M. Grätzel, Nature 353 (1991) 737.
[2] M. Grätzel, Nature 414 (2001) 338.
[3] K. Hara, T. Horiguchi, T. Kinoshita, K. Sayama, H. Sugihara, H. Arakawa, Sol. Energy Mater. Sol. Cells 64 (2000) 115.
[4] Y. Chiba, A. Islam, Y. Watanabe, R. Komiya, N. Koide, L. Han, Jpn. J. Appl. Phys. 45 (2006) L638.
[5] Z.-S. Wang, T. Yamaguchi, H. Sugihara, H. Arakawa, Langmuir 21 (2005) 4272.
[6] M.K. Nazeeruddin, F. De Angelis, S. Fantacci, A. Selloni, G. Viscardi, P. Liska, S. Ito, B. Takeru, M. Grätzel, J. Am. Chem. Soc. 127 (2005) 16835.
[7] T. Toyoda, T. Sano, J. Nakajima, S. Doi, S. Fukumoto, A. Ito, T. Tohyama, M. Yoshida, T. Kanagawa, T. Motohir, T. Shiga, K. Higuchi, H. Tanaka, Y. Takeda, T. Fukano, N. Katoh, A. Takeichi, K. Takechi, M. Shiozawa, J. Photochem. Photobiol. A 164 (2004) 203.
[8] M. Ikegami, J. Suzuki, K. Teshima, M. Kawaraya, T. Miyasaka, Sol. Energy Mater. Sol. Cells 93 (2009) 836.
[9] Q. Wang, J.-E. Moser, M. Grätzel, J. Phys. Chem. B 109 (2005) 14945.
[10] S.Y. Huang, G. Schlichthörl, A.J. Nozik, M. Grätzel, A.J. Frank, J. Phys. Chem. B 101 (1997) 2576.
[11] L. Dloczik, O. Ileperuma, I. Lauermann, L.M. Peter, E.A. Ponomarev, G. Redmond, N.J. Shaw, I. Uhlendorf, J. Phys. Chem. B 101 (1997) 10281.
[12] R. Kern, R. Sastrawan, J. Ferber, R. Stangl, J. Luther, Electrochim. Acta 47 (2002) 4213.
[13] F. Cao, G. Oskam, G.J. Meyer, P.C. Searson, J. Phys. Chem. B 100 (1996) 17021.
[14] M. Itagaki, A. Taya, K. Watanabe, K. Noda, Anal. Sci. 18 (2002) 641.
[15] M. Itagaki, I. Shitanda, W. Nakamura, K. Watanabe, Electrochim. Acta 52 (2007) 6421.
[16] M. Itagaki, N. Kobari, S. Yotsuda, K. Watanabe, S. Kinoshita, M. Ue, J. Power Sources 135 (2004) 255.
[17] M. Itagaki, S. Suzuki, I. Shitanda, K. Watanabe, H. Nakazawa, J. Power Sources 161 (2007) 415–424.
[18] L. Han, N. Koide, Y. Chiba, T. Mitate, Appl. Phys. Lett. 84 (2004) 2433.
[19] T. Hoshikawa, R. Kikuchi, K. Eguchi, J. Electroanal. Chem. 558 (2006) 59.
[20] L. Han, N. Koide, Y. Chiba, A. Islam, R. Komiya, N. Fuke, A. Fukui, R. Yamanaka, Appl. Phys. Lett. 86 (2005) 213501.
[21] T. Hoshikawa, M. Yamada, R. Kikuchi, K. Eguchi, J. Electroanal. Chem. 577 (2005) 339.
[22] T. Hoshikawa, R. Kikuchi, K. Sasaki, K. Eguchi, Electrochemistry 70 (2002) 675.
[23] T. Hoshikawa, M. Yamada, R. Kikuchi, K. Eguchi, J. Electrochem. Soc. 152 (2005) E68.
[24] T. Hoshikawa, T. Ikebe, M. Yamada, R. Kikuchi, K. Eguchi, J. Photochem. Photobiol. A Chem. 184 (2006) 78.
[25] M. Adachi, M. Sakamoto, J. Jiu, Y. Ogata, S. Isoda, J. Phys. Chem. B 110 (2006) 13872.
[26] N. Fuke, A. Fukui, R. Komiya, A. Islam, Y. Chiba, M. Yanagida, R. Yamanaka, L. Han, Chem. Mater. 20 (2008) 4974.
[27] N. Kato, Y. Takeda, K. Higuchi, A. Takeichi, E. Sudo, H. Tanaka, T. Motohiro, T. Sano, T. Toyoda, Sol. Energy Mater. Sol. Cells 93 (2009) 893.
[28] J. Tornow, K. Ellmer, J. Szarko, K. Schwarzburg, Thin Solid Films 516 (2008) 7139.
[29] D. Kuang, S. Ito, B. Wenger, C. Klein, J.-E. Moser, R. Humphry-Baker, S.M. Zakeeruddin, M. Grätzel, J. Am. Chem. Soc. 128 (2006) 4146.
[30] D. Kuang, P. Wang, S. Ito, S.M. Zakeeruddin, M. Grätzel, J. Am. Chem. Soc. 128 (2006) 7732.
[31] R. Sastrawan, J. Renza, C. Prahl, J. Beier, A. Hinsch, R. Kern, J. Photochem. Photobiol. A Chem. 178 (2006) 33.
[32] D. Kuang, C. Klein, S. Ito, J.-E. Moser, R. Humphry-Baker, S.M. Zakeeruddin, M. Grätzel, Adv. Funct. Mater. 17 (2007) 154.
[33] J. Tornow, K. Schwarzburg, J. Phys. Chem. C 111 (2007) 8692.
[34] M.C. Bernard, H. Cachet, P. Falaras, A. Hugot-Le Goff,a, M. Kalbac, I. Lukes, N.T. Oanh,a,d, T. Stergiopoulos, I. Arabatzis, J. Electrochem. Soc. 150 (2003) E155.
[35] C. Longo, A.F. Nogueira, M.-A. De Paoli, H. Cachet, J. Phys. Chem. B 106 (2002) 5925.
[36] J. Bisquert, G. Garcia-Belmonte, F. Fabregat-Santiago, N.S. Ferriols, P. Bogdanoff, E.C. Pereira, J. Phys. Chem. B 104 (2000) 2287.
[37] J. Bisquert, J. Phys. Chem. B 106 (2002) 325.
[38] A. Zaban, A. Meier, B.A. Gregg, J. Phys. Chem. B 101 (1997) 7985.
[39] J. van de Lagemaat, N.-G. Park, A.J. Frank, J. Phys. Chem. B 104 (2000) 2044.
[40] J. Bisquert, V.S. Vikhrenko, J. Phys. Chem. B 108 (2004) 2313.
[41] F.F. Santiago, G.G. Belmonte, J. Bisquert, A. Zaban, P. Salvador, J. Phys. Chem. B 106 (2002) 334.
[42] K. Schwarzburg, F. Willig, J. Phys. Chem. B 107 (2003) 3552.
[43] P. Balraju, M. Kumar, M.S. Roy, G.D. Sharma, Synth. Met. 159 (2009) 1325.
[44] T.-S. Kang, K.-H. Chun, J.-S. Hong, S.-H. Moon, K.-J. Kim, J. Electrochem. Soc. 147 (2000) 3049.
[45] F.F. Santiago, J.G. Cañadas, E. Palomares, J.N. Clifford, S.A. Haque, J.R. Durrant, G.G. Belmonte, J. Bisquert, J. Appl. Phys. 96 (2004) 6903.
[46] P.J. Cameron, L.M. Peter, J. Phys. Chem. B 107 (2003) 14394.
[47] B.P. Nelson, R. Candal, R.M. Corn, M.A. Anderson, Langmuir 16 (2000) 6094.
[48] T.-V. Nguyen, H.-C. Lee, O.-B. Yang, Sol. Energy Mater. Sol. Cells 90 (2006) 967.
[49] N. Koide, A. Islam, Y. Chiba, L. Han, J. Photochem. Photobiol. A Chem. 182 (2006) 296.
[50] L. Bay, K. West, Sol. Energy Mater. Sol. Cells 87 (2005) 613.
[51] D. Kuang, J. Brillet, P. Chen, M. Takata, S. Uchida, H. Miura, K. Sumioka, S.M. Zakeeruddin, M. Grätzel, ACS Nano 2 (2008) 1113.
[52] P. Cheng, C. Deng, D. Liu, X. Dai, Appl. Surf. Sci. 254 (2008) 3391.
[53] C.-P. Hsu, K.-M. Lee, J.-T.-W. Huang, C.-Y. Lin, C.-H. Lee, L.-P. Wang, S.-Y. Tsai, K.-C. Ho, Electrochim. Acta 53 (2008) 7514.
[54] X. Li, H. Lin, J. Li, X. Li, B. Cui, L. Zhang, J. Phys. Chem. C 112 (2008) 13744.
[55] H.C. Weerasinghe, P.M. Sirimanne, G.P. Simon, Y.B. Cheng, J. Photochem. Photobiol. A Chem. 206 (2009) 64.
[56] T. Stergiopoulos, A. Valota, V. Likodimos, Th. Speliotis, D. Niarchos, P. Skeldon, G.E. Thompson, P. Falaras, Nanotechnology 20 (2009) 365601.
[57] K.-M. Lee, C.-W. Hu, H.-W. Chen, K.-C. Ho, Sol. Energy Mater. Sol. Cells 92 (2008) 1628.
[58] M.S. Roy, P. Balraju, M. Kumar, G.D. Sharma, Sol. Energy Mater. Sol. Cells 92 (2008) 909.
[59] K. Lee, S. Park, M. Jae Ko, K. Kim, N. Gyu Park, Nat. Mater. 28 (2009) 665.
[60] C. He, L. Zhao, Z. Zheng, F. Lu, J. Phys. Chem. C 112 (2008) 18730.
[61] J. Weidmann, Th. Dittrich, E. Konstantinova, I. Lauermann, I. Uhlendorf, F. Koch, Sol. Energy Mater. Sol. Cells 56 (1999) 153.
[62] Z. Zhang, S.M. Zakeeruddin, B.C. O'Regan, R. Humphry-Baker, M. Grätzel, J. Phys. Chem. B 109 (2005) 21818.
[63] C. He, Z. Zheng, H. Tang, L. Zhao, F. Lu, J. Phys. Chem. C 113 (2009) 10322.
[64] J.-J. Wu, G.-R. Chen, H.-H. Yang, C.-H. Ku, J.-Y. Lai, Appl. Phys. Lett. 90 (2007) 213109.
[65] N.-G. Park, K.M. Kim, M.G. Kang, K.S. Ryu, S.H. Chang, Y.-J. Shin, Adv. Mater. 17 (2005) 2349.
[66] T. Sawatsuk, A. Chindaduang, C.S. Kung, S. Pratontep, G. Tumcharern, Diam. Relat. Mater. 18 (2009) 524.
[67] W. Song, W. Xiaohong, Q. Wei, J. Zhaohua, Electrochim. Acta 53 (2007) 1883.
[68] N. Papageorgiou, W.F. Maier, M. Grätzel, J. Electrochem. Soc. 144 (1997) 876.
[69] A. Hauch, A. Georg, Electrochim. Acta 46 (2001) 3457.
[70] T. Ma, X. Fang, M. Akiyama, K. Inoue, H. Noma, E. Abe, J. Electroanal. Chem. 574 (2004) 77.
[71] G. Wang, R. Lin, Y. Lin, X. Li, X. Zhou, X. Xiao, Electrochim. Acta 50 (2005) 5546.
[72] M. Ikegami, K. Miyoshi, T. Miyasaka, K. Teshima, T.C. Wei, C.C. Wan, Y.Y. Wang, Appl. Phys. Lett. 90 (2007) 153122.
[73] G. Khelashvili, S. Behrens, C. Weidenthaler, C. Vetter, A. Hinsch, R. Kern, K. Skupien, E. Dinjus, H. Bönnemann, Thin Solid Films 511–512 (2006) 342.
[74] C.-H. Yoon, R. Vittal, J. Lee, W.-S. Chae, K.-J. Kim, Electrochim. Acta 53 (2008) 2890.
[75] K.-M. Lee, P.-Y. Chen, C.-Y. Hsu, J.-H. Huang, W.-H. Ho, H.-C. Chenc, K.-C. Ho, J. Power Sources 188 (2009) 313.
[76] W.J. Lee, E. Ramasamy, D.Y. Lee, J.S. Song, Sol. Energy Mater. Sol. Cells 92 (2008) 814.
[77] C.-P. Lee, K.-M. Lee, P.-Y. Chen, K.-C. Ho, Sol. Energy Mater. Sol. Cells 93 (2009) 1411.
[78] L. Bay, K. West, B. Wither-Jensen, T. Jacobsen, Sol. Energy Mater. Sol. Cells 90 (2006) 341.
[79] T.C. Wei, C.C. Wan, Y.Y. Wang, Appl. Phys. Lett. 88 (2006) 103122.
[80] F.F. Santiago, J. Bisquert, G.G. Belmonte, G. Boschloo, A. Hagfeldt, Sol. Energy Mater. Sol. Cells 87 (2005) 117.
[81] M.A.K.L. Dissanayake, L.R.A.K. Bandara, R.S.P. Bokalawala, P.A.R.D. Jayathilaka, O.A. Ileperuma, S. Somasundaram, Mater. Res. Bull. 37 (2002) 867.
[82] F.F. Santiago, J. Bisquert, E. Palomares, L. Otero, D. Kuang, S.M. Zakeeruddin, M. Grätzel, J. Phys. Chem. C 111 (2007) 6550.

[83] G. Kron, T. Egerter, J.H. Werner, U. Rau, J. Phys. Chem. B 107 (2003) 3556.
[84] S. Chengwu, D. Songyuan, W. Kongjia, P. Xu, G. Li, Z. Longyue, H. Linhua, K. Fantai, Sol. Energy Mater. Sol. Cells 86 (2005) 527.
[85] G. Kron, T. Egerter, G. Nelles, A. Yasuda, J.H. Werner, U. Rau, Thin Solid Films 403–404 (2002) 242.
[86] C. Shi, S. Dai, K. Wang, X. Pan, L.Z.L. Hu, F. Kong, L. Guo, Electrochim. Acta 50 (2005) 2597.
[87] L. Andrade, S.M. Zakeeruddin, M.K. Nazeeruddin, H.A. Ribeiro, A. Mendes, M. Grätzel, Int. J. Chem. Eng. 7 (2009) 1.
[88] J. Zhang, Y. Yang, S. Wu, S. Xu, C. Zhou, H. Hu, B. Chen, H. Han, X. Zhao, Electrochim. Acta 53 (2008) 5415.
[89] J. Xia, N. Masaki, M.L. Cantu, Y. Kim, K. Jiang, S. Yanagida, J. Am. Chem. Soc. 130 (2008) 1258.
[90] J.P. Lee, B. Yoo, T.S.M.S. Kang, R. Vital, K.J. Kim, Electrochim. Acta 54 (2009) 4365.
[91] C. Zafer, K. Ocakoglu, C. Ozsoy, S. Icli, Electrochim. Acta 54 (2009) 5709.
[92] C.-W. Tu, K.-Y. Liu, A.-T. Chien, M.-H. Yen, T.-H. Weng, K.-C. Ho, K.-F. Lin, J. Polym. Sci. Polym. Chem. 46 (2008) 47.
[93] T.-C. Wei, C.-C. Wan, Y.-Y. Wang, Sol. Energy Mater. Sol. Cells 91 (2007) 1892.
[94] Z. Huo, S. Dai, K. Wang, F. Kong, C. Zhang, X. Pan, X. Fang, Sol. Energy Mater. Sol. Cells 91 (2007) 1959.
[95] M. Zistler, C. Schreiner, P. Wachter, P. Wasserscheid, D. Gerhard, H.J. Gores, Int. J. Electrochem. Sci. 3 (2008) 236.
[96] C.-W. Tu, A.-T. Chien, C.-H. Lee, K.-C. Ho, K.-F. Lin, Eur. Polym. J. 44 (2008) 608.
[97] Y. Zhao, X. Sheng, J. Zhai, L. Jiang, C. Yang, Z. Sun, Y. Li, D. Zhu, Chem. Phys. Chem. 8 (2007) 856.
[98] Y. Zhao, J. Zhai, J. He, X. Chen, L. Chen, L. Zhang, Y. Tian, L. Jiang, D. Zhu, Chem. Mater. 20 (2008) 6022.
[99] J. Halm, M. Toivola, A. Tolvanen, P. Lund, Sol. Energy Mater. Sol. Cells 90 (2006) 872.
[100] Y. Yoshida, S. Tokashiki, K. Kubota, R. Shiratuchi, Y. Yamaguchi, M. Kono, S. Hayase, Sol. Energy Mater. Sol. Cells 92 (2008) 646.
[101] B. Yoo, K. Kim, S.H. Lee, W.M. Kim, N.G. Park, Sol. Energy Mater. Sol. Cells 92 (2008) 873.
[102] J.-H. Park, Y. Jun, H.-G. Yun, S.-Y. Lee, M.-G. Kang, J. Electrochem. Soc. 155 (2008) F145.
[103] S. Lee, J.H. Noh, S.-T. Bae, I.-S. Cho, J.Y. Kim, H. Shin, J.-K. Lee, H.S. Jung, K.S. Hong, J. Phys. Chem. C 113 (2009) 7443.
[104] Y. Jun, M.G. Kang, J. Electrochem. Soc. 154 (2007) B68.
[105] J. Ferber, R. Stangl, J. Luther, Sol. Energy Mater. Sol. Cells 53 (1998) 29.
[106] S. Tanaka, Jpn. J. Appl. Phys. 40 (2001) 97.
[107] J.R. Bastida, Field Eextensions and Galois Theory, Encyclopedia of Mathematics and its Applications, vol. 22, Addision-Wesley: Reading, Massachusetts, 1984.
[108] G. Arfken, Mathematical Methods for Physicists, 3rd ed., Academic Press, San Diego, 1985.
[109] K. Seeger, Semiconductor Physics, Springer Series in Solid State Science, vol. 40, Springer, Berlin, 1982.
[110] V.A. Macagno, M.C. Giordano, A.J. Arvia, Electrochim. Acta 14 (1969) 335.
[111] L.M. Dané, L.J.J. Janssen, J.G. Hoogland, Electrochim. Acta 13 (1968) 507.
[112] A.J. Bard, L.R. Faulkner, Electrochemical Methods, John Wiley and Sons, New York, 1980.
[113] A. Zaban, J. Zhang, Y. Diamant, O. Melemed, J. Bisquert, J. Phys. Chem. B 107 (2003) 6022.
[114] H. Gerischer, M.E. Michel-Beyerle, F. Rebentrost, H. Tributsch, Electrochim. Acta 13 (1968) 1509.
[115] I. Epelboin, M. Keddam, J.C. Lestrade, Disc. Faraday Soc. 56 (1973) 264.
[116] M. Koelsch, S. Cassaignon, C. Ta Thanh Minh, J.-F. Guillemoles, J.-P. Jolivet, Thin Solid Films 451–452 (2004) 86.
[117] K. Imoto, K. Takahashi, T. Yamaguchi, T. Komura, J.I. Nakamura, K. Murata, Sol. Energy Mater. Sol. Cells 79 (2003) 459.